Galactic archaeology: Describing stellar structures in galaxies via 2D photometric decompositions

Arqueología galáctica: Describiendo estructuras estelares en galaxias usando decomposiciones fotométricas en 2D

Autora
Lucía Fernández Arroyo

Tutor
Sébastien Comerón Limbourg

Contents

List of Tables

List of Figures

Resumen general

La *Spitzer* Survey of Stellar Structures in Galaxies (S^4G) consiste en una muestra de imágenes profundas a 3.6 y 4.5 μm de 2352 galaxias, tomadas con el instrumento Infrared Array Camera (IRAC) instalado en el Telescopio Espacial *Spitzer* (Sheth et al. 2010). La selección de galaxias está basada en su velocidad radial ($V_{\text{radio}} < 3000$ km/s), así como en la magnitud total en B corregida ($m_{B\text{corr}} < 15.5$ mag), el diámetro angular isofotal ($D_{25} > 1'.0$) y la latitud Galáctica ($|b| > 30°$), según los datos recogidos en HyperLEDA (Paturel et al. 2003). Sin embargo, la muestra presenta un sesgo importante. Debido a que las velocidades radiales fueron tomadas de fuentes que caracterizaban la línea de HI, se excluyeron, mayoritariamente, galaxias de tipo temprano con bajo contenido en gas (con velocidad radiales tomadas en el rango óptico). Por este motivo, el equipo de S^4G llevó a cabo una muestra adicional de 465 galaxias (extensión de Early Type Galaxies, o de ETGs) con los mismos criterios que la original (Sheth et al. 2013) pero con velocidad radial medida a partir de espectros en el óptico, con el fin de rellenar aquellos tipos morfológicos tempranos que no se pudieron estudiar originalmente.

La pipeline de la S^4G original consta de cinco partes: la Pipeline 1 (P1, Regan 2013) se basa en el tratamiento de las imágenes original; la Pipeline 2 (P2, Muñoz-Mateos et al. 2015) en la creación de máscaras para dichas imágenes, en caso de objetos que las puedan afectar; en la Pipeline 3 (P3, Muñoz-Mateos et al. 2015) se derivan perfiles radiales de parámetros globales de las galaxias (tamaño, magnitud, color, etc.); en la Pipeline 4 (P4, Salo et al. 2015) se realizan descomposiciones fotométricas de las estructuras galácticas, y en la Pipeline 5 (P5, Querejeta et al. 2015b) se corrigen las imágenes finales por contaminantes (por ejemplo, polvo caliente). Sin embargo, para la extensión de ETGs se han publicado resultados hasta la P3 (Watkins et al. 2022). En este trabajo se han realizado descomposiciones fotométricas en dos dimensiones de la extensión con GALFIT (Peng et al. 2002, Peng et al. 2010), siguiendo los criterios establecidos para las descomposiciones en la P4 de la S^4G original, y es fundamental para la futura publicación de la P4 de la extensión.

Los modelos fotométricos finales para cada galaxia se construyeron a partir de cuatro funciones distintas: función de Sérsic, disco exponencial, perfil de Ferrers modificado y psf. En las descomposiciones está permitido usar cualquier combinación de estas funciones, pero están limitadas a un máximo de cuatro componentes, y se realizaron para todas las imágenes disponibles, excepto para las galaxias con orientación de canto. Los modelos finales para cada galaxia tienen asociado un criterio de calidad (quality flag, QF) que indica el grado de fiabilidad del modelo y que varía entre 1 y 5. Aquellas galaxias con criterio 1 o 2 (en resumen, aquellas cuyas imágenes originales no son de buena calidad o con morfología muy distorsionada) fueron excluidas. Finalmente, se obtuvieron 380 descomposiciones válidas para su posterior análisis.

La parte final de este trabajo se centra en el análisis de parámetros derivados de las distintas estructuras de las galaxias, con el fin de entender la naturaleza de las mismas. Para ello, se agrupan las galaxias en su tipo de Hubble y se realiza la estadística para cada tipo de la fracción de luminosidad del bulbo (B/T), el índice de Sérsic, la fracción de luminosidad de las barras (Bar/T), y la longitud de escala (h_{r}) y brillo superficial central de los discos (μ_0), todo en función del tipo de Hubble. Este análisis conduce a una discusión sobre los tipos de bulbo (clásicos y pseudobulbos) que se pueden encontrar en las galaxias de la extensión, así como la posible influencia de las barras en los parámetros derivados de los discos (h_{r} y μ_0). Adicionalmente, también se discute la distribución de tipos morfológicos de la muestra y de los distintos tipos de modelos usados.

Los modelos obtenidos para la muestra original de S^4G también tienen importancia en este trabajo. La comparación de estos con los derivados para la extensión permite descubrir sesgos en la creación de modelos de ambas muestras: aunque se han intentado seguir los mismos criterios que en la P4 original, también se ha considerado que i) los modelos de galaxias elípticas pueden contener más de un pérfil de Sérsic y ii) se ha intentado modelar las partes externas de las galaxias con discos adicionales. Este último

punto entra en conflicto con uno de los razonamientos de la P4 original, que asume que un único disco exponencial es suficiente para una primera estimación de lo parámetros del disco de una galaxia (aunque en casos excepcionales se usa más de un disco exponencial). A la hora de derivar la longitud de escala y el brillo superficial central se optó por considerar los discos más externos. Esta decisión no afecta al propio análisis de las ETGs (al menos dentro del alcance de este trabajo) pero sí a la comparación de las muestras. Debido a esto, también se presentan los resultados de estos mismos parámetros pero usando el disco interno.

En las conclusiones se recogen los resultados más importantes obtenidos en este trabajo. En cuanto a las galaxias de la extensión de ETGs, se discuten los valores de los párametros calculados, además de cómo la propia morfología de las galaxias puede llegar a afectarlos (p.e, la presencia de pseudobulbos y la influencia de las barras en los párametros de los discos). La comparación con las galaxias de la S^{4}G, como se ha comentado anteriormente, resalta los sesgos en las descomposiciones de ambas muestras: en particular para las elípticas y las galaxias con disco. Es necesario revisar estas peculiaridades antes de plantear un análisis definitivo de todas las galaxias, pero esto no minimiza la importancia de las descomposiciones fotométricas realizadas para la publicación de la Pipeline 4 de la extensión de ETGs. Finalmente, se indica una posible línea de estudio adicionale: la influencia de los anillos estelares sobre las descomposiciones.

Chapter 1

Introduction

1.1 The *Spitzer* survey of stellar structure in galaxies $(\mathrm{S}^4\mathrm{G} + \mathrm{ETG})$

The Spitzer Survey of Stellar Structures in Galaxies (S^{4}G) is a survey of 2352 nearby galaxies at 3.6 and 4.5 μm with the Infrared Array Camera (IRAC) at the *Spitzer* Space Telescope (Sheth et al. 2010). These wavelengths are broadly unaffected by internal extinction (Draine & Lee 1984) and are excellent tracers of old stellar populations (Pahre et al. 2004). The mass-to-luminosity ratio (M/L) is nearly constant in galaxies for these bands (Peletier et al. 2012), which is key for understanding the properties of bulges and disks: dust and star formation are more relevant in the disks than in the bulges, which has an effect in the bulge-to-total fraction estimates in the optical (Driver et al. 2013).

The galaxies that were selected for the survey have a radial velocity $V_{\mathrm{radio}} < 3000$ km/s (equivalent to a distance $d < 40$ Mpc for a Hubble constant of 75 km/s/Mpc), total corrected blue magnitude $m_{B\mathrm{corr}} < 15.5$ mag, blue light isophotal angular diameter $D_{25} > 1'.0$ at Galactic latitude $|b| > 30°$ as reported in the HyperLEDA database (Paturel et al. 2003). Each galaxy was observed for 240 seconds and images reach a surface brightness $\mu_{3.6} \sim 26$ mag arcsec^{-2} in AB, which is equivalent to a stellar mass surface density of $\sim 1 M_\odot \mathrm{pc}^{-2}$. The original choice of V_{radio} introduces a bias in the sample towards gas-rich late-type galaxies (LTGs), as it misses some galaxies for which only optically derived radial velocities are available. As a result small, early-type galaxies (ETGs) as well as some small, faint galaxies were excluded from the initial sample. The S^{4}G Team carried out a supplementary *Spitzer* survey of 465 ETGs so as to fill the existing morphological gaps (Sheth et al. 2013). The bands and selection criteria were identical to those for the original S^{4}G, and IRAC was also used. The full survey to date is known as S^{4}G + ETG and contains 2817 galaxies.

The original S^{4}G pipeline is divided into five parts: Pipeline 1 (P1, Regan 2013) transforms the raw data files into sciente-ready data, Pipeline 2 (P2, Muñoz-Mateos et al. 2015) builds a mask for each galaxy that accounts for the foreground and background objects, Pipeline 3 (P3, Muñoz-Mateos et al. 2015) measures global properties of each galaxy (size, axial ratio, magnitude, color, etc.) and computes the radial profiles of each of the aforementioned properties, Pipeline 4 (P4, Salo et al. 2015) breaks down each galaxy into its major structural components, and Pipeline 5 creates mass maps of the images corrected for hot dust and other contaminants (P5, Querejeta et al. 2015b) These methods have been applied, up to P3, to the ETG extension (Watkins et al. 2022). The aim of this work is to proceed with the ETG's analysis with a similar approach to the original Pipeline 4.

1.2 The *Spitzer* Space Telescope and IRAC

The *Spitzer* Space Telescope (SST) was launched on the 25th of August of 2003. It was the final mission in NASA's Great Observatories program, which consisted of a family of four space-based observatories planned to observe in different wavelength ranges. The other three were the *Hubble* Space Telescope, the *Compton* Gamma Ray Observatory and the *Chandra* X-ray Observatory. The SST was designed to
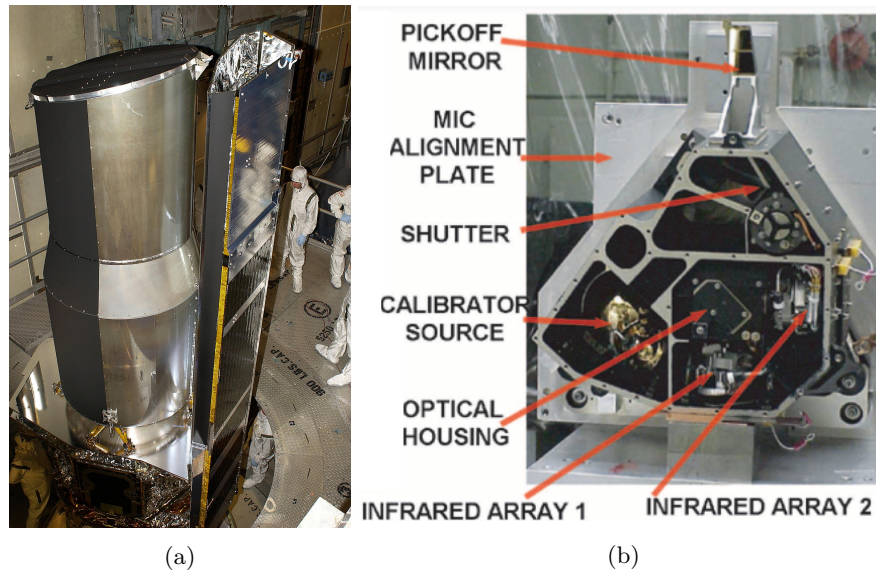
(a)   (b)

Figure 1.1: a) The *Spitzer* Telescope before launch. Credits: NASA/JPL-Caltech, b) IRAC with some labelled components (image taken from Fazio et al. 2004).

operate in the infrared region of the electromagnetic spectrum, filling the wavelength gaps in which Earth-based telescopes cannot observe at due to water absorption by the Earth's atmosphere and also its own emission. The *Spitzer* Telescope (Werner et al. 2004) incorporated a 85 cm diameter mirror and three instruments: the Infrared Array Camera (IRAC), the Infrared Spectrograph (IRS) and the Multiband Imaging Photometer for Spitzer (MIPS), and all of them used liquid helium in order to cool the sensors to as low as 5.5 K. The SST was originally built to last for a minimum of 2.5 years in its cold phase (that is, with available liquid helium) but the cooling fuel lasted for 5.5 years. After that, the SST entered its warm phase, in which only two wavelengths (3.6 and 4.5 μm) could still be observed with IRAC, as the channels did not need to be cooled down as much. The telescope was finally retired on January of 2020.

IRAC (Fazio et al. 2004) is a four-channel camera that takes broadband images simultaneously at 3.6, 4.5, 5.8 and 8.0 μm. It was designed to study the early universe, in particular the evolution of galaxies up to $z < 3$ with deep, large-area surveys. It has a large field of view (two almost adjacent $5'.2 \times 5'.2$ FOVs viewed by the four channels in pairs) and high sensitivity, making it a powerful instrument for this type of survey. IRAC data (together with data provided by the other two instruments) has been used extensively in a wide range of science programs, both for extragalactic and galactic research. Some examples are the Formation and Evolution of Planetary Systems (FEPS), the *Spitzer* IRAC Equatorial Survey (SpIES) and the Cosmic Dawn Survey.

1.3 The morphology and formation of Early Type Galaxies

In 1926, Edwin Hubble proposed the popular and extensively used morphological classification of galaxies known as Hubble's sequence (Hubble 1926). It was originally based on the optical appearance of galaxy images on photographic plates and organises galaxies into three categories: ellipticals (En, n indicates the ellipticity of the galaxy), spirals (S or SB, B indicates the presence of a bar), and irregulars (Irr). The latter do not appear on the version of his diagram published in 1936 (Figure 1.2) because at the time it was considered that they did not present any signs of rotational symmetry and could not be placed in the diagram. Lenticular galaxies (S0s) are included as a necessary stage between ellipticals and spirals. At the time, it was erroneously thought that Hubble's diagram explained the time evolution of galaxies and it was considered a sequence (hence the name of the classification) originating from ellipticals that evolved into spirals after being lenticulars. For this reason, E and S0s are known as early-type (ETGs) and spirals as late-type galaxies (LTGs), even though galaxy evolution is substantially more complex

than it was believed at the time and does not follow the original interpretation of Hubble's diagram.
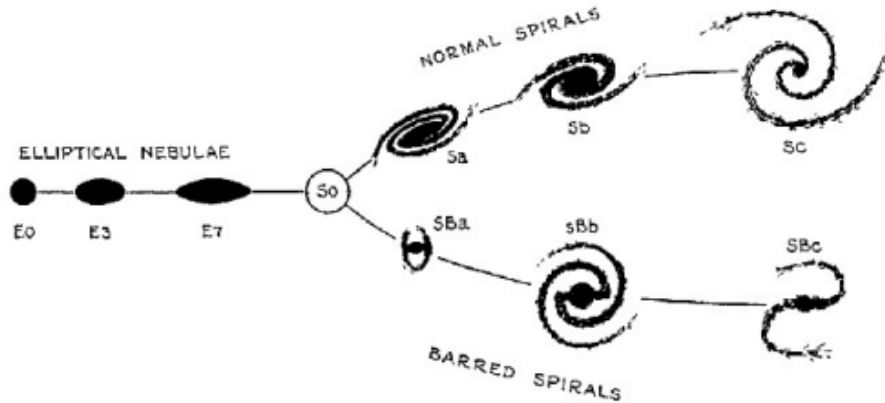
Figure 1.2: "The Sequence of Nebular Types" diagram (Hubble 1936)

In 1976, Sidney van den Bergh proposed a revised galaxy classification system which includes a sequence for spiral galaxies, parallel to that of normal spirals (van den Bergh 1976). The two sequences differ in their total gas content and therefore on the mean age of their stellar populations. He also contemplated the existence of a sequence of intermediate objects to spirals and lenticulars, which he named gas-poor "anemic" spirals. The sequence of lenticulars was divided in S0a, S0b and S0c (see Figure 1.3). This subdivision is based on the relative fraction of the central bulge and of the disk.
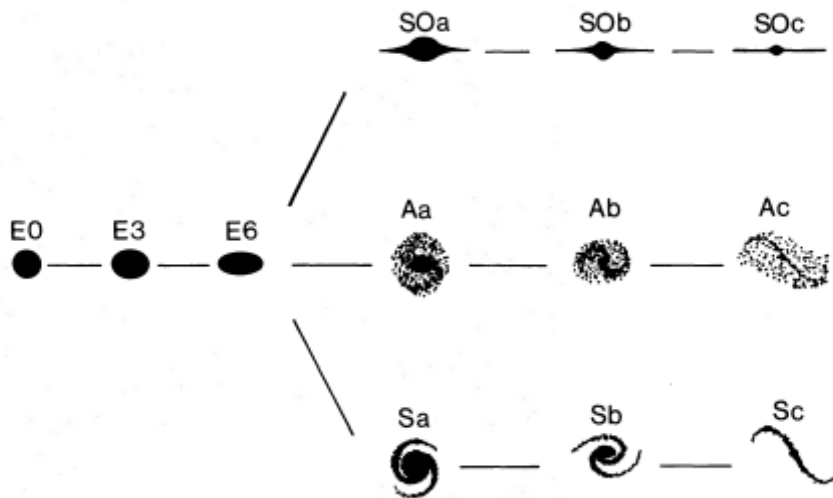
Figure 1.3: Galaxy classification proposed by van den Bergh (1976).

Early-type galaxies are gas- and dust-poor, and dominated by old stellar populations. This term includes both the disk-dominated and rotation-supported lenticular galaxies, and the pressure-supported ellipticals. Different mechanisms have been proposed for the formation of both lenticular and elliptical galaxies. Due to the similarities between S0s and late-type spirals (bulge-to-total mass or light ratios, range of bulge luminosities, bar properties, and kinematics, e.g. Laurikainen et al. 2011) it is speculated that the former may have evolved from LTGs through the removal or rapid consumption of gas and dust. S0s are relatively abundant in galaxy clusters, so one possible mechanism may involve the infall of a LTG into a dense environment (e.g., Dressler 1980). Isolated field S0s, although rare, do exist, so cluster infall must not be the only formation pathway. More recently, Falcón-Barroso et al. (2019) argued that

simple quenching and fading of stellar populations may not be sufficient to explain S0 formation, and simulations favor mergers to describe S0 kinematics (Querejeta et al. 2015a).

The origin of elliptical galaxies is also complex. The first theories were based on a monolithic collapse (Eggen et al. 1962), but with the surging of ΛCDM cosmology a hierarchical formation was favoured (Franx et al. 1991). Varying merger histories indeed appear to be essential for understanding elliptical's lack of rotation (supported by simulations, e.g. Cappellari et al. 2011) and diversity of core profiles. The dominant type of merger pathway remains unknown, although a series of complex minor mergers is preferred over major interactions (Bournaud et al. 2007), and the formation tracks of ellipticals seem to be mass-dependent. More recently, Oser et al. (2010) suggested a two-phase scenario for ETG formation. The first step is an early and short-lived period of star formation in the ETG progenitor, similar to the monolithic collapse proposed by Eggen et al. (1962), also known as 'cold flow-driven' star formation (e.g., Dekel & Birnboim 2006). This is followed by a merger-dominated period involving dry accretion of neighbouring systems. The two-phase scenario is supported by observations of passively-evolving ETGs at high redshift that are more compact than the ones found locally (e.g, Daddi et al. 2005) and by the characterisation of the evolution of ETG envelopes (e.g, Ryan et al. 2012).

Chapter 2

Objectives

The objectives of this work are twofold. The main goal is to create 2D photometric decompositions of infrared images into different stellar structures, using GALFIT, for the ETG extension of the original S^{4}G survey. These are essential for the completion and release of the ETG extension Pipeline 4, which will be parallel to P4 of the original S^{4}G survey and will fill the morphological gaps that resulted from the bias towards gas-rich LTGs. The scope of this work allows for a first statistical analysis of some bulge, bar and disk parameters obtained from said photometric decompositions. This is necessary for a preliminary understanding of the nature of the ETG extension galaxies. In order to fill the morphological gaps in the S^{4}G survey with the results obtained in this work, it is necessary to identify possible biases in the building of the final models. These biases arise when comparing the structural properties of both surveys, and have to be accounted for before a comprehensive analysis of the merging of the two surveys is established.

Chapter 3

Methodology

3.1 Photometric decompositions with GALFIT

The decompositions for the ETG extension were done using GALFIDL, which consists of IDL-based tools for displaying and running GALFIT (Peng et al. 2002, Peng et al. 2010) and following criteria from Salo et al. (2015) (P4). GALFIT is routinely used to produce two-dimensional structural decompositions and is based on parametric fitting, using the Levenberg-Marquadt algorithm to minimise the weighted residual χ^2_ν between the observed and model images. The P4 decompositions for the original S^{4}G use five different options for the model components.

1. A Sérsic profile for the bulge ("*sersic*")

$$\Sigma(r) = \Sigma_{\mathrm{e}} \exp\left(-\kappa\left[(r/R_{\mathrm{e}})^{1/n} - 1\right]\right), \tag{3.1}$$

   where Σ_{e} is the surface brightness at the effective radius R_{e} (isophotal radius in which half of the total flux of the component is contained). The Sérsic index n defines the shape of the radial profile, which is steeper for increasing n: $n = 0.5$ matches a Gaussian profile, $n = 1$ an exponential profile and $n = 4$ a de Vaucouleurs profile. κ is a normalization parameter that depends on n. In GALFIT, the integrated magnitude m_{bulge} is used as a free parameter, instead of Σ_{e}.

2. A disk with a low or moderate inclination is described using a infinitessimaly thin exponential disk ("*expdisk*")

$$\Sigma(r) = \Sigma_0 q^{-1} \exp\left(-r/h_{\mathrm{r}}\right) \tag{3.2}$$

   where Σ_0 is the central surface brightness of the disk (from the perpendicular direction) and h_{r} is the exponential scale length. Also, $q = \cos i$, where i is the disk inclination. For a disk with no extinction, $\Sigma_0 q^{-1}$ is the projected central surface brightness at the sky plane. In GALFIT, the integrated magnitude $m_{\mathrm{disk}} = -2.5 \log_{10}\left(2\pi\Sigma_0 h_r^2\right)$ is used as a free parameter, instead of Σ_0.

3. A nearly edge-on disk is described with the "*edgedisk*" function

$$\Sigma\left(r_x, r_z\right) = \Sigma_0 \frac{r_x}{h_{\mathrm{r}}} \mathrm{K}_1\left(\frac{r_x}{h_{\mathrm{r}}}\right) \mathrm{sech}^2\left(r_z/h_z\right) \tag{3.3}$$

   where r_x and r_z are the distances along and perpendicular to the apparent major axis of the disk, and K_1 is a modified Bessel function.

4. A modified Ferrers profile ("*ferrer2*")is adopted for describing a bar component

$$\Sigma(r) = \begin{cases} \Sigma_0\left[1 - (r/r_{\mathrm{out}})^{2-\beta}\right]^{\alpha} & r < r_{\mathrm{out}} \\ 0 & r \geqslant r_{\mathrm{out}} \end{cases} \tag{3.4}$$

   where r_{out} sets the outer cut of the profile. The parameters α and β define the sharpness of the cut and the central slope of the profile, respectively, and Σ_{o} is the central surface brightness (in the plane of the sky).

5. An unresolved central component can be fitted with a PSF-convolved point source ("*psf*"), using $m_{\rm psf}$ as a free parameter. It usually corresponds to a small bulge or an AGN with an angular size so small that cannot be resolved in the S^{4}G images.

The pipeline distinguishes three types of decompositions: 1-component Sérsic fits, 2-component bulge-disk decompositions using Sérsic-bulges and exponential disks (or edge-on disks in necessary), and multicomponent "final" decompositions. The first two types are done automatically and are available for both the original S^{4}G and the ETG extension. The multicomponent models need human judgement to be completed and are finished/published for the original S^{4}G (Salo et al. 2015).

3.1.1 Generation of Input Files for GALFIT

The input file (ascii) for GALFIT includes the paths to the galaxy data, mask, sigma, and PSF-fits files, as well as the region of the data image selected for the decompositions. An example of an input file is included in Appendix B. The images used as input correspond to the galaxy data at 3.6μm. The sigma images establish the weights applied in GALFIT decompositions by quantifying the statistical uncertainty of each image pixel, which has two contributions: the noise contribution (or photon noise, related to the number of photons arriving at the instrument) and the noise introduced by the instrument. The photon noise is related to the flux associated with the galaxy light and the flux from the sky background, and is assumed to follow a Poission distribution. The wavefront of light coming from distant sources always presents perturbations by the act of producing an image: that is, distortions due to imperfect optics or by diffraction. This results in the blurring of the image, and it must be taken into account when comparing a model with the intrinsic shape of an object. In image fitting, it is usually done by convolving a model image with the input PSF before comparing with the data. This process, particularly for GALFIT, is described thoroughly in Peng et al. (2010). It is also noted that when the data are oversampled, the convolution of the model can be done correctly if the PSF provided to GALFIT is also oversampled. This is the case for the IRAC data, as the FWHM of the PSF is $2\rlap{.}''1$, which is much larger than the S^{4}G $0\rlap{.}''75$(see Comerón et al. 2018) pixel. The IRAC PSF also shows wide wings, so a large convolution box size must be used in decompositions: it is set to $40'' \times 40''$. Details on the final oversampled PSF can be found in Salo et al. (2015). GALFIT convolves this PSF with a model created on a finer grid and then bins the result down to the resolution of the data, allowing a comparison.

The components/functions used in the model are specified in the input file, as well as the initial guesses for the parameters and whether they are fixed or not. The ones that are not fixed are iteratively varied to minimize χ_ν^2, although this value is not used as an indicator of the goodness of the fit (a simple model is preferred over a small χ_ν^2). The number and nature of the components were chosen manually and the centers of each of them were fixed to the galaxy center. The output files are generated after convergence and can be used as input files if convenient, as their format is very similar.

Some parameters had to be fixed and then released to obtain the final model (e.g for elliptical galaxies with more than one *sersic* profile in the model). The outer truncation radius of some models containing the *ferrer2* function had to be kept fixed: if not, GALFIT returned a model with a bar that did not match the observed image. This was checked by visual inspection of the original image and the generated model. In other cases, fixing this radius before completing the model and then releasing it produced a satisfactory model. If a galaxy could be modelled with one "*expdisk*", its axis ratio and position angle were fixed in the input file. This was also applied to the outermost disk in galaxies with more than one "*expdisk*", so that the disk orientation was fixed to the shape of the outer isophotes determined from the images, which are taken from Watkins et al. (2022). For the inner disk(s) this parameters were freed or was/were modelled with a *ferrer2* function in some cases.

The statistical uncertainties of the decompositions parameters are related to image noise under the assumption that the derived model is accurately describing the true light distribution of the galaxy and will not be further discussed in this study.

Function	Parameters		
	Fixed	Free	Fixed/free
sersic	position, (x, y)	integrated magnitude, μ	
	effective radius, R_{e}		
	Sérsic index, n		
	axis ratio, b/a		
	position angle, PA		
expdisk	position, (x, y)	integrated magnitude, μ	axis ratio, b/a
		disk scale length, R_{s}	position angle, PA
ferrer2	position, (x, y)	surface brightness at effective radius, μ_e	outer truncation radius, R_{out}
	α	axis ratio, b/a	
	β	position angle, PA	
psf	position, (x, y)	integrated magnitude, μ	

Table 3.1: GALFIT decomposition parameters for the four functions that were used. These could be either fixed and/or freed when creating the input files, as indicated in the table. The axis ratio (b/a) and position angle (PA) of the inner disk could be freed if there was an outer disk (in which those parameters were fixed). The outer truncation radius of the bar (R_{out}) was fixed when GALFIT returned an incorrect model for the bar. $\alpha = 2$ and $\beta = 0$ for all model components with *ferrer2* function (see Equation 3.4). The output GALFIT files contain the fitted values, and some of them were used for the final analysis.

3.1.2 Final Multi-Component Decompositions

The final decompositions for the galaxies in the ETG extension were created by fitting a maximum of four components (in any combination of them): the bulge (b), disk (d), bar (bar or barf, whether the length was a free or a fixed parameter), and nucleus (n). As in Salo et al. (2015), the labelling of the component is based on interpretation of the component, not the function used in the fit. The name of the input and output files indicate the selected components for the final model. Once again, decompositions were based on criteria established in Salo et al. (2015) (P4), albeit a different approach towards ellipticals was taken. The original S^{4}G study focused on the analysis of disk galaxies, so even though it was considered that many elliptical galaxies can be fitted with a combination of Sérsic components (Huang et al. 2013), ellipticals are modelled with either a single Sérsic component or a Sérsic profile and an exponential disk. In this study, focused on the ETG extension, multiple Sérsic components were considered when creating the decompositions for elliptical galaxies, as well as the inclusion of an unresolved central component. Some decompositions are single- or two-component models but in the majority of cases the automatic models were not selected as the final fit. Also, decompositions were partially based on the visual classification in the middle-infrared in the Comprehensive de Vaucouleurs revised Hubble-Sandage (CVRHS) system by Buta et al. (2002). This system follows the classical de Vaucouleurs classification, but it also recognises features such as lenses, nuclear rings, X patterns and box/peanut structures, barlenses, etc. The classifications for the ETG extension galaxies can be found in Watkins et al. (2022).

The original ETG extension consists of 465 galaxies, but the data of five of them were not available for this study. Of the 460 available galaxies, 59 are edge-on and thus not analysed, resulting in a set of 401 modelled galaxies. Each final model was assigned a quality flag (QF) to indicate the trustworthiness of the derived structural parameters, as some decompositions for the galaxies in the sample are not very reliable or cannot be carried out at all. This was based on the criteria followed by Salo et al. (2015). A brief summary of these criteria is indicated below, as well as the number of the 401 modelled galaxies that fit into each category.

1. **Quality flag = 1 (14)** Bad original data (overlapping stars, varying background, image defects). A model was derived but excluded from analysis.

2. **Quality flag = 2 (7)** The original data is somewhat fine but sky estimation is not reliable or the galaxy shows strongly distorted morphology (mergers, peculiar shapes, strong warps, lopsidedness). A model was derived but excluded from analysis.

3. **Quality flag = 3 (19)** The original data is fine. The galaxy has complex structures that need a more detailed analysis (e.g, more than four components for the final model or other functions).

4. **Quality flag = 4 (51)** The original data and decompositions are of good quality, but there is a degeneracy between model components due to the complex structure of the galaxy.

5. **Quality flag = 5 (310)** The original data is of good quality and the final decompositions are adequate.

Galaxies with QF=1 and QF=2 were not considered in the final analysis, but their recurrence is low: for a total of 401 modelled galaxies, only 21 were excluded, leaving 380.

The name, final decomposition model, quality flag, Hubble type and the luminosity fraction of each component for each galaxy were registered into a data table (an excerpt of this table is included in Appendix A), as well as all the values of the parameters listed in Table 3.1. These were extracted directly from the GALFIT output files. The results of the original S^{4}G survey were subsequently added to the table and each galaxy was labelled in order to identify whether they belong to the original S^{4}G or the ETG extension. This was done for the latter comparison and discussion of the results of both surveys.

3.1.3   Decomposition examples

Examples of the final decompositions are depicted for NGC 3636, NGC 3226, ESO 548-047, NGC 4697 and NGC 3945, all from the ETG extension. These galaxies were selected to show the variety of models that were built and as a reference on how the QFs were assigned.

NGC 3636 (Figure 3.1) is an example of a galaxy with QF = 1 that was not considered in the statistical analysis, as the original data is sub-par: the original image (Figure 3.1a) is dominated by an overlapping star and the subsequent masked image (Figure 3.1b) excludes a significant part of the galaxy. However, it was modelled with two Sérsic profiles acting as two distinct spheroid components (Figure 3.1e). Galaxies that were assigned a QF=2 were also not considered in the final analysis, and NGC 3226 (Figure 3.2) is one of those. In this case, the original data is acceptable but NGC 3226 is interacting with another galaxy (Figure 3.2a), NGC 3227. The resulting masked image (Figure 3.2b) hides the non-targeted galaxy, but the effects of the interaction can still be noted on NGC 3226. Again, a model was created for this galaxy with one Sérsic function, acting as a spheroid component, and an unresolved central component (Figure 3.2e), but it was not used in further analysis.

Figure 3.3 shows the final decomposition for ESO 548-047, which consists of a Sérsic profile and an exponential disk. This galaxy is an example of those with QF=3 because the available functions are not enough to describe the galaxy's brightness profile and the resulting final model is not as satisfactory as the ones with a higher quality flag. NGC 4697 final model is composed of two Sérsic functions (Figure 3.4), but there is a clear degeneracy between them: that is, in some regions (in this case, the outer region), the components cannot be differentiated in the resulting brightness curve. For this reason, it was assigned a QF=4. The final model for NGC 3945 (see Figure 3.5) contains four components ("BDDBAR"), which is the maximum number of structures allowed for the decompositions. It was assigned a QF=5: this is because the final model is adequate, taking into account the limitation of using only four different functions to model the brightness profile.
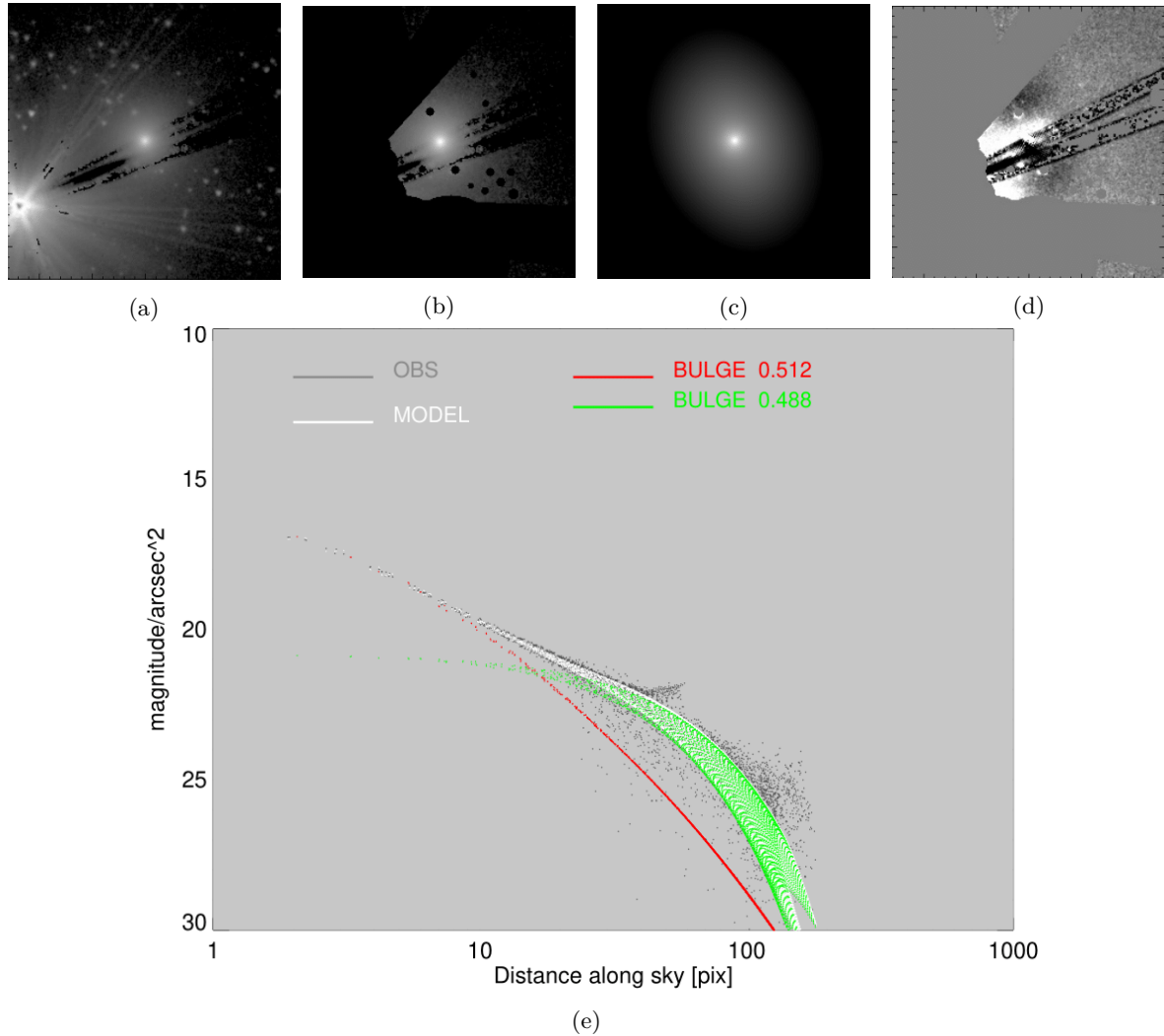
(a)   (b)   (c)   (d)

(e)

Figure 3.1: Figures 3.1 to 3.5 show the final decompositions described in Subsection 3.1.3. The top four panels show the a) original image at 3.6 μm; b) masked image, c) model image and d) the residual (original-model) image, where white denotes excess light over the model. The final panel e) is the 2D profile of the original (grey dots) and model (white dots) images. The contribution of each component is portrayed in different colour dots. The luminosity fraction of each component is also indicated. This is example is for NGC 3636, a $T = -5$ and QF = 1 galaxy which was modelled using two Sérsic functions ("BB").

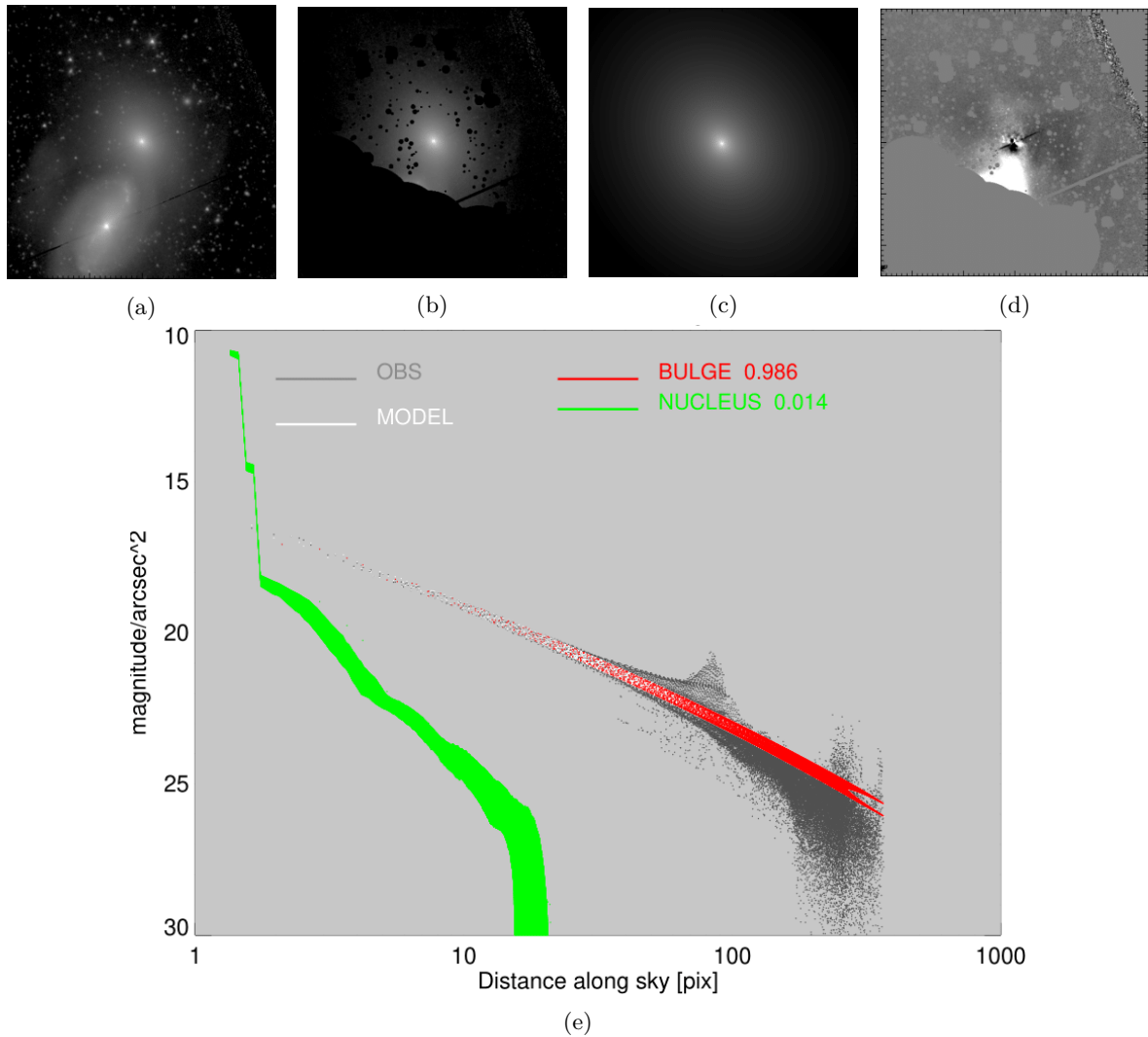(a)   (b)   (c)   (d)

(e)

Figure 3.2: Distribution of the panels as in Figure 3.1. The final model for NGC 3226 (T = -5 and QF = 2) consists of a Sérsic function and a nucleus (or PSF-convolved point source), "BN".
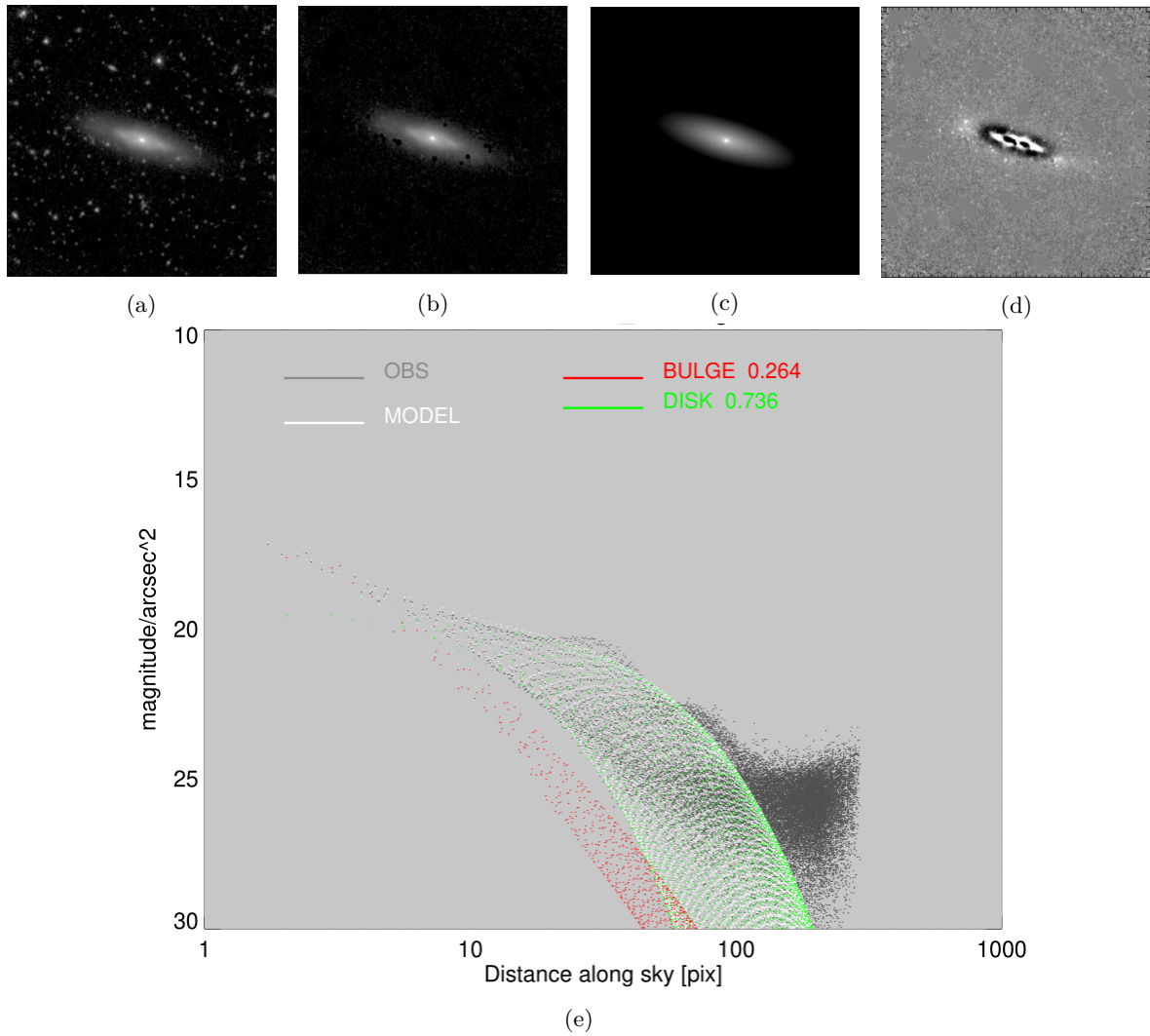
(a)   (b)   (c)   (d)

(e)

Figure 3.3: Distribution of the panels as in Figure 3.1. The final model for ESO 548-047 (T = -1 and QF = 3) consists of a Sérsic function and an exponential disk, "BD".

(a)

(b)

(c)

(d)

(e)
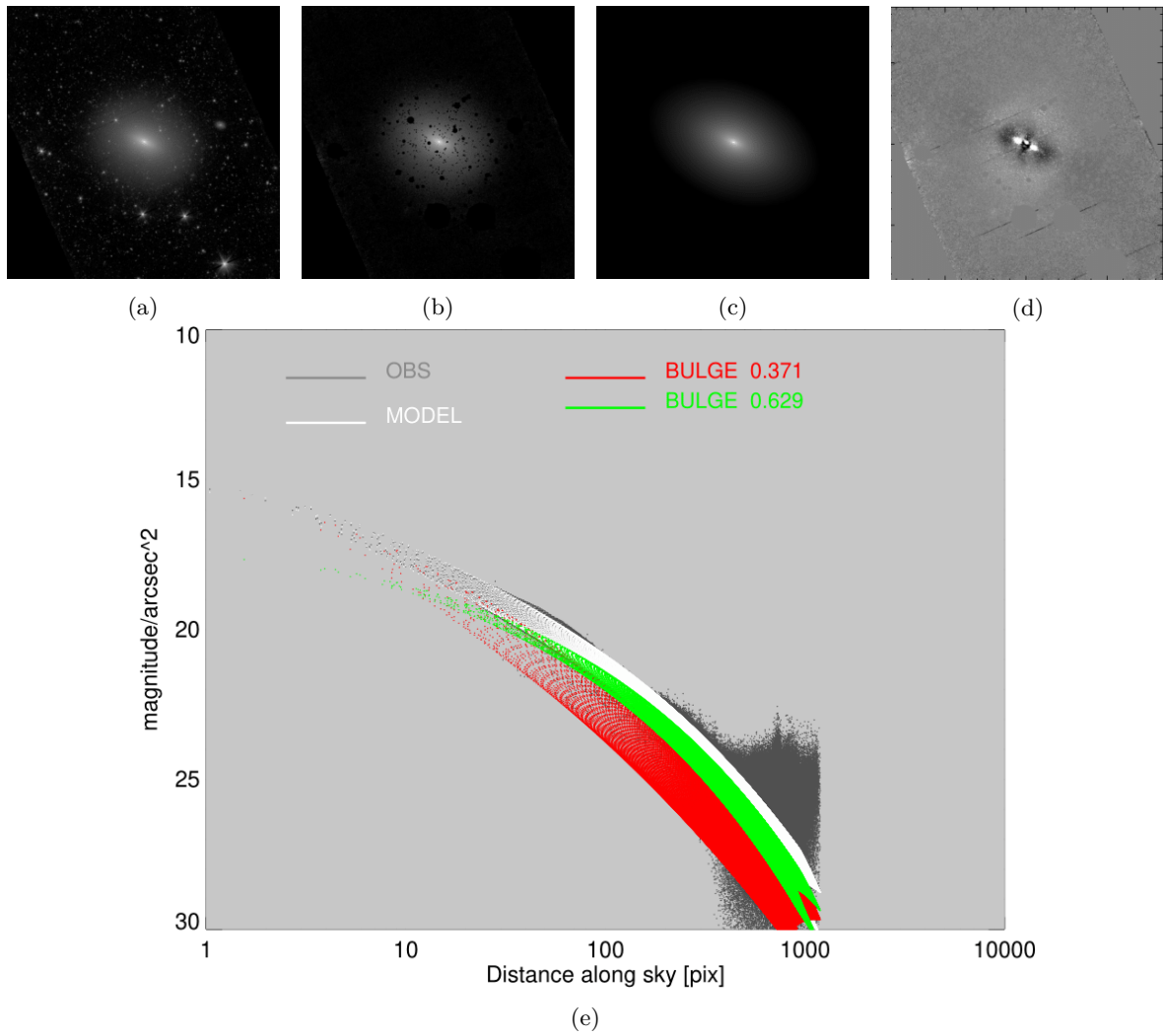
Figure 3.4: Distribution of the panels as in Figure 3.1. The final model for NGC 4697 (T = -5 and QF = 4) consists of two Sérsic functions, "BB".
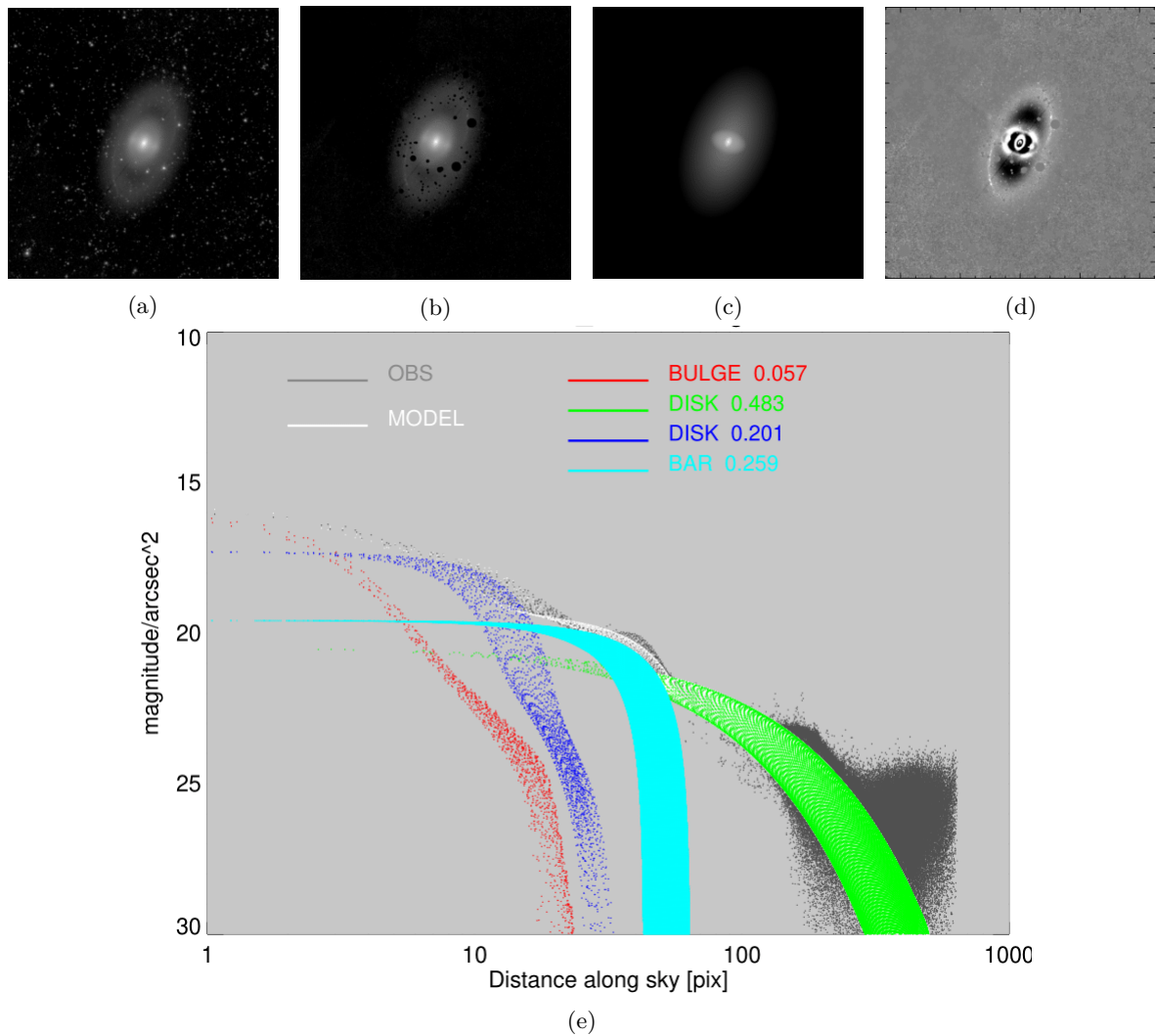
(a)   (b)   (c)   (d)

(e)

Figure 3.5: Distribution of the panels as in Figure 3.1. The final model for NGC 3945 ($T = -1$ and QF = 5) was built using a Sérsic function, two exponential disks and a modified Ferrers profile, "BDDBAR".

14

Chapter 4

Results

4.1 ETG analysis
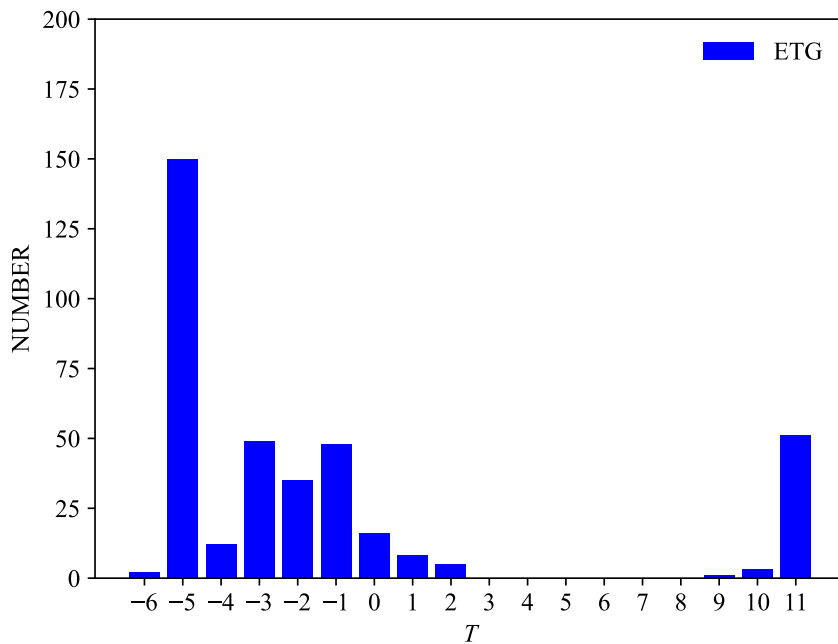
Figure 4.1: T-type ocurrences in the ETG final sample.

The number of galaxies with models that could be considered for the final analysis is 380, as explained in Subsection 3.1.2. The vast majority of them are classified with T-types (see Table 4.1) between $T = -5$ and $T = 2$, with an important peak at $T = -5$. Galaxies with $T = -6, 9, 10$ and 11 (adding up to 57 galaxies) are also included in the analysis but the results focus on types ranging from $T = -5$ to $T = 2$.

Stage	Numerical index (T-type)
cE	-6
E	-5
E$^+$	-4
S0$^-$	-3
S0^0	-2
S0$^+$	-1
S0/a	0
Sa	1
Sab	2
Sb	3
Sbc	4
Sc	5
Scd	6
Sd	7
Sdm	8
Sm	9
Im	10
dE, dS0, dSph	11

Table 4.1: Numerical T-types
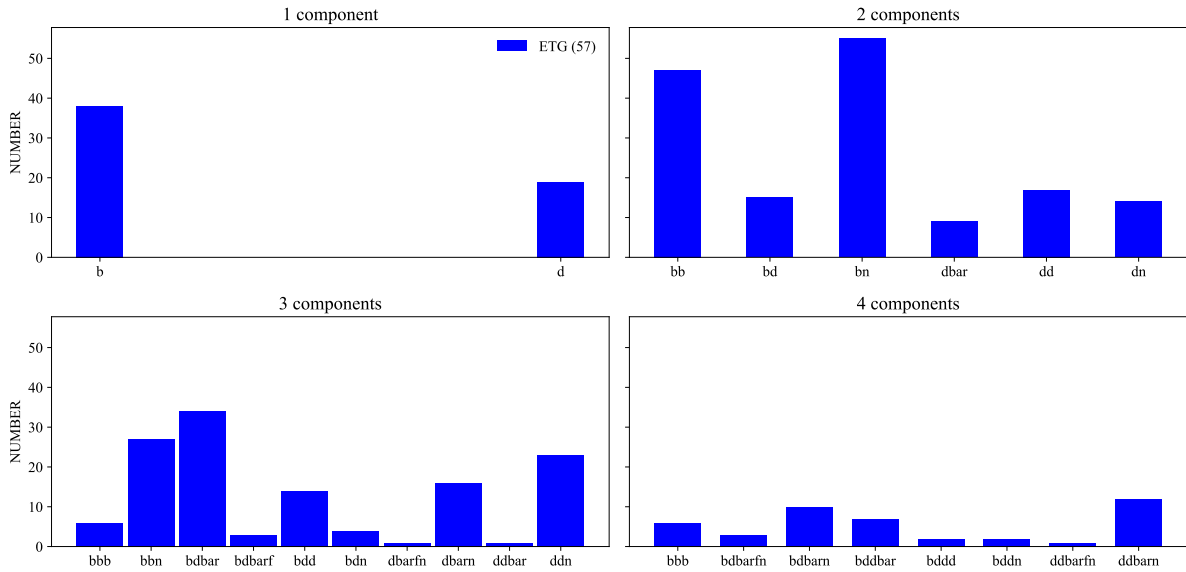
Figure 4.2: Model distribution of the ETG final sample.

The final decompositions range from one to a maximum of four components, with any combination of the functions described in Section 3.1. The distribution of the nature of the final models is depicted in Figure 4.2. The most recurrent models are those with two components, with those named "BN" being the most frequently used (a fourth of all ellipticals ($T = -5$ and $T = -4$) were modelled with it).

The study of the different structural parameters results in the creation of a series of samples that do not necessarily contain the same galaxies, as the selection is based on the different components of the models. The name and reasoning behind each sample will be specified in the corresponding Subsections, but Table 4.2 summarizes the samples used for the ETG analysis.

Name	Parameter	Number of galaxies
ETG extension - Sample I	Bulge luminosity fraction (galaxies with at least a bulge or nucleus component)	332
ETG extension - Sample I.a	Sérsic index (galaxies with at least a bulge component)	260
ETG extension - Sample II	Bar luminosity fraction (galaxies with at least a bar component)	95
ETG extension - Sample III	Disk scale length and central surface brightness (galaxies with at least a disk component)	205

Table 4.2: Samples of ETG galaxies used in the analysis. The name, the parameter that it was selected to study and the number of galaxies in the sample is indicated.

4.1.1 Bulge to total luminosity

The bulge luminosity fraction or (bulge to total luminosity, B/T) for each galaxy was calculated by adding the luminosity fraction(s) of the bulge(s) and the nucleus component[1], in case they were present in the final decomposition. The result of this selection is a sample of 332 galaxies (Sample I) for which B/T could be obtained. The galaxies were then sorted according to their Hubble type, in order to determine the mean B/T for each stage and its associated error. Sample I was divided into two main categories, barred and non-barred galaxies, as seen in Figure 4.3. Earlier, non-barred types are almost all "bulge" ($T = -5$ and $T = -4$ correspond to ellipticals), so B/T is close to or unity. On the other hand, the B/T value decreases rapidly (below 0.4) for later types than $T = -4$.

Figure 4.3: Bulge luminosity fraction as a function of Hubble type for Sample I of the ETG extension. The values are compared for barred and non-barred galaxies. The symbols indicate the mean value of the galaxies in each bin and error bars correspond to the error of the mean. Non-filled symbols indicate that the bin contains more than one galaxy; filled ones only contain one object and no error bar is displayed.

Galaxies with one or more Sérsic functions acting as "bulge" were selected from Sample I, excluding those which only contain an unresolved central component that contributes to the value of B/T (hence the difference in number of galaxies between Sample I and Sample I.a). The mean of the different n was used to represent each galaxy and then they were again assorted according to their Hubble type, and the mean n was determined for each stage, as well as the associated error. Sample I.a was also divided into

---

[1]The presence of a nucleus in the model introduces a bias: the luminosity of the bulge could be overestimated if the unresolved central component is actually an AGN.
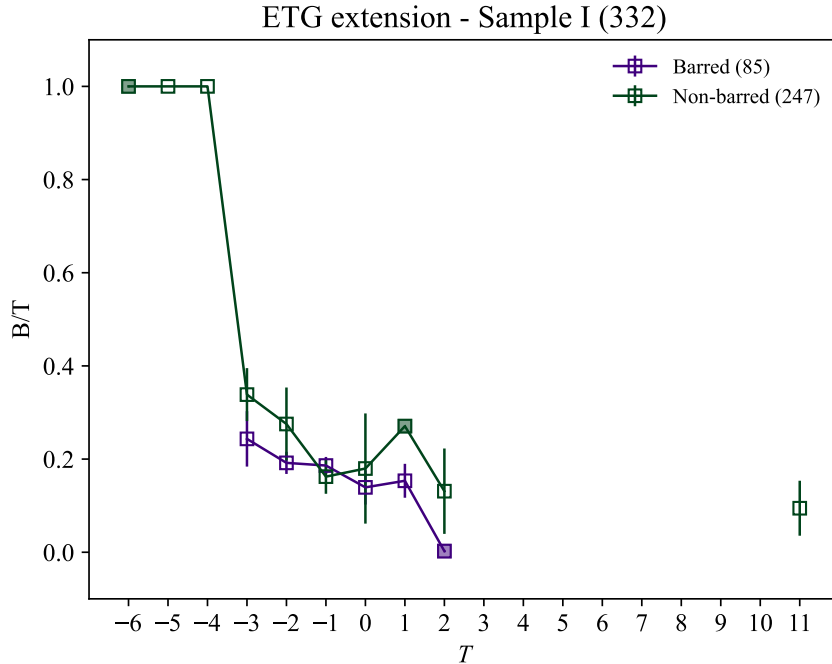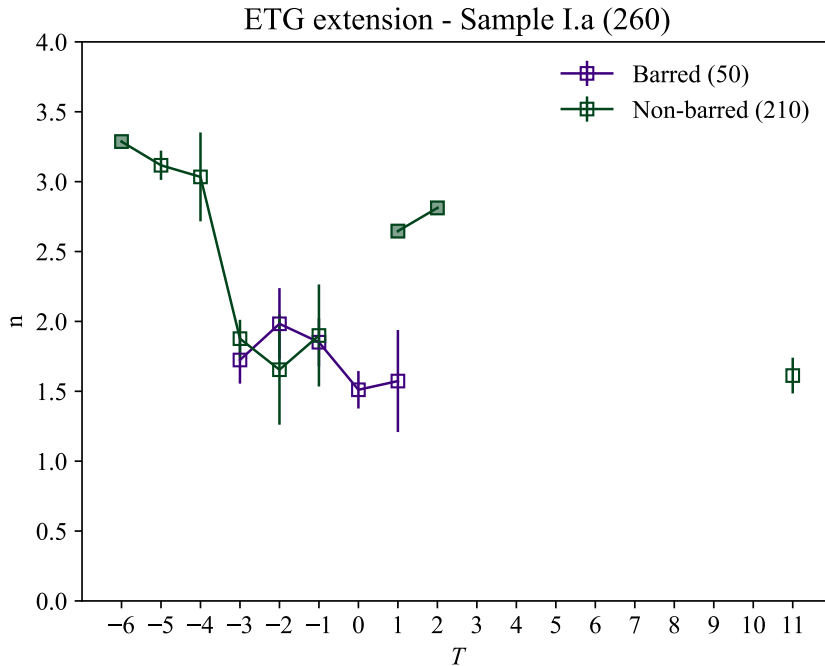
Figure 4.4: Sérsic index as a function of Hubble type for Sample I.a of the ETG extension. The values are compared for barred and non-barred galaxies. Symbols as in Figure 4.3.

barred and non-barred galaxies (see Figure 4.4). Galaxies with $T = -5$ and $T = -4$ present the highest n values ($n \approx 3$). For later types, the mean Sérsic index drops to $n = 2$ and below.

The behaviour of both the B/T and the Sérsic index for the ETGs samples could be explained by the nature of the bulge. Classical bulges (those more similar to elliptical galaxies) are expected in early, non-barred galaxies and are thought to be formed by hierarchical clustering (via minor mergers). Pseudo-bulges, on the other hand, are associated to later types (often barred) and to disk instabilities and slow secular evolution processes within them. This formation scenario was first proposed by Kormendy (1982) and the main observational criteria for identifying pseudo-bulges are listed in Kormendy & Kennicutt (2004). The ones that are relevant in the framework of this study are (i) the presence of a nuclear bar, (ii) a Sérsic index $n = 1-2$ (Fisher & Drory 2008 claim a turnover index $n = 2$), and (iii) B/T lower than 0.5.

The use of Sérsic indices to describe pseudo-bulges is prone to ambiguity, and sometimes the use of the Kormendy relation (Kormendy 1977) is preferred[2], but this goes far beyond the scope of this work. However, based on the observational criteria listed previously and the evidence presented in Figure 4.3 and Figure 4.4, pseudo-bulges could be present in galaxies with $T > -3$. The presence of a bar could also affect the B/T ratios when dealing with pseudo-bulges, as discussed in Laurikainen et al. (2007): B/T is slightly smaller for barred galaxies because it is possible for parts of the pseudo-bulge to blend with the bars.

4.1.2 Bar to total luminosity

The bar luminosity fraction (or bar to total luminosity, Bar/T) for each galaxy was determined in a similar manner as the bulge luminosity fraction (see Subsection 4.1.1) but using instead the bar component. The result of this selection is a sample of 95 galaxies (Sample II) for which Bar/T was obtained. The galaxies

---

[2]The Kormendy relation is based on the well-defined relation in massive elliptical galaxies between the mean effective surface brightness within the effective radius and the effective radius.
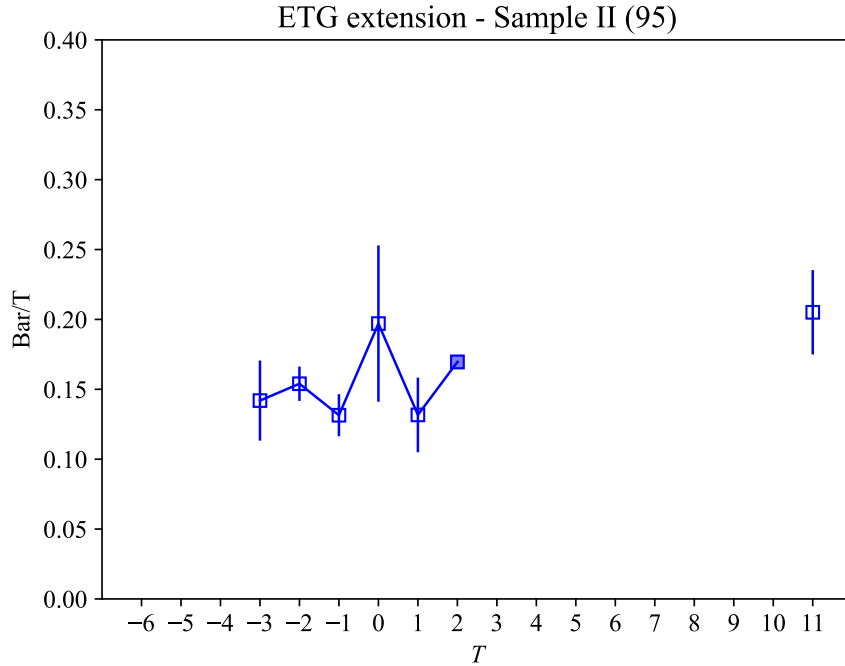
Figure 4.5: Bar luminosity fraction as a function of Hubble type for Sample II of the ETG extension. Symbols as in Figure 4.3.

were then assorted according to their Hubble type, so as to obtain the mean Bar/T and associated error for each morphological stage. There were no galaxies with more than one bar component, so it was not necessary to sum the contribution of different bar components. Figure 4.5 shows the results of this analysis. The bar luminosity fractions for the available T types fall into the same range, approximately between 0.10 and 0.20, but without a significant trend.

4.1.3 Disk properties

The disky structure in galaxies of the ETG sample were predominantly modelled with one exponential disk component. However, when building the final decompositions, it was sometimes necessary to add an additional exponential disk to better describe the innermost or outermost regions of some galaxies. As stated in Section 3.1.1, the outermost disk of models containing one or more "*expdisk*" functions has its orientation fixed to the outer isophotes determined from the original images of the galaxies. The disk scale length of this peripheral component is used to study the size of the disk in relation to the Hubble type classification of each galaxy (see Figure 4.6). This consideration is also taken into account in the study of the outermost disk's central surface brightness (Figure 4.7.)

Both the disk scale lengths recorded in the GALFIT output files are given in arcseconds. In order to get the physical value of the galaxies' sizes it is necessary to convert this parameter into kiloparsecs using the following expression:

$$h_\mathrm{r}[\mathrm{kpc}] = \frac{h_\mathrm{r}[\mathrm{arcsec}] \times D[\mathrm{kpc}]}{206265} \tag{4.1}$$

Both the disk scale length and central surface brightness were averaged for each Hubble type, and the related errors were also calculated. Galaxies were classified into barred and non-barred and also according to the number of disks present in the final models. The resulting sample (Sample III) consists of 205 galaxies.
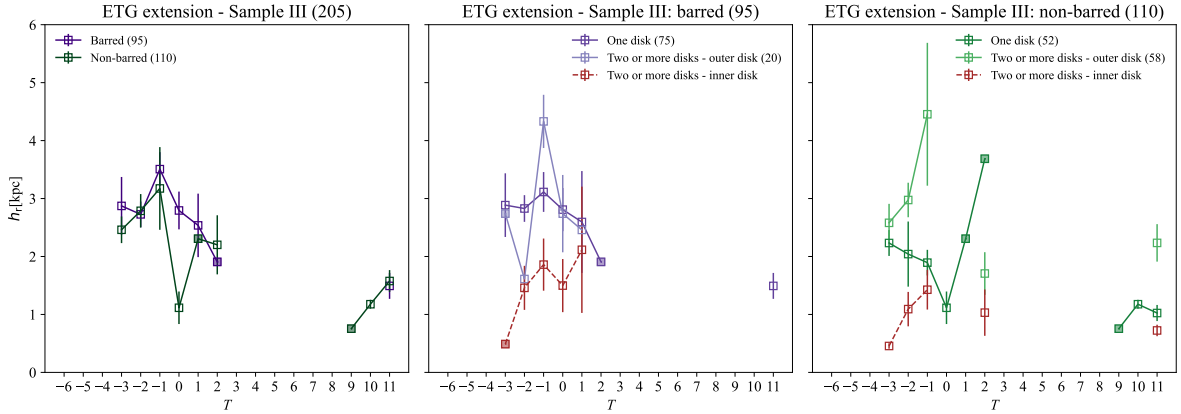
Figure 4.6: Disk scale length as a function of Hubble type for Sample III of the ETG extension. The first panel compares the values for barred and non-barred galaxies. The second and third panel compares the disk scale lengths for models with one or two more disks in the model for barred and non-barred galaxies, respectively. Symbols as in Figure 4.3. Non-dashed lines indicate the behaviour of the only disk in the model or the outer one, in models that contain more than one exponential disk. The dashed, red lines in the second and third panel indicate the behaviour of inner disk, in models that contain more than one disk.

Figure 4.6 shows the values of the disk scale lengths for barred and non-barred galaxies of the only disk in the galaxy or the outer one, in case there were more than one disk in the model (non-dashed values). As a comparison, the values for the inner disk (again, in case of more than one disk) are included (red, dashed values) in the second and third panel of the same Figure. It is noticeable the decrease in the disk scale length when using the inner disk, for both barred and non-barred galaxies. The analysis, as originally intended, will be centered in the outer disk. The disk scale lengths for barred galaxies seem to be larger than for non-barred galaxies, as shown in the first panel of Figure 4.6. This could be a direct effect of the presence of the bar: the mass redistribution triggered by this type of structure can increase notably the disk scale length of the host galaxy (e.g, Hohl 1971; Athanassoula & Misiriotis 2002).

The values of the central surface brightness for Sample III are shown in Figure 4.7, for the only disk in the galaxy or the outer one, in case there were more than one disk in the model (non-dashed values), and for barred and non-barred galaxies. Once more, as a comparison, the values for the only disk or the inner one (again, in case of more than one disk) are included (red, dashed values) in the second and third panel of the same Figure. The values for the inner disk are brigther, as inner regions of the galaxy are being modelled with this component. As for the disk scale lengths, the analysis is centered in the outer disks. Non-barred galaxies have lower central surface brightness (first panel of Figure 4.7). The brightness of the disks in barred galaxies is prone to be more concentrated towards the center of the disk, as the central surface brightness values are higher. There is strong support for the idea that bar-driven gas inflow towards the center of galaxies triggers star formation (e.g, Lin et al. 2017), and as shown by nuclear rings of star formation (Comerón et al. 2010), so this could explain the higher central surface brightness values found for barred galaxies. For non-barred galaxies (third panel of Figure 4.7) central surface brightness values are quite similar, independently of the number of disks used in the model. For barred galaxies this behaviour also applies to $T < 0$, but for types later than $T = 0$, values for models with one disk are higher.
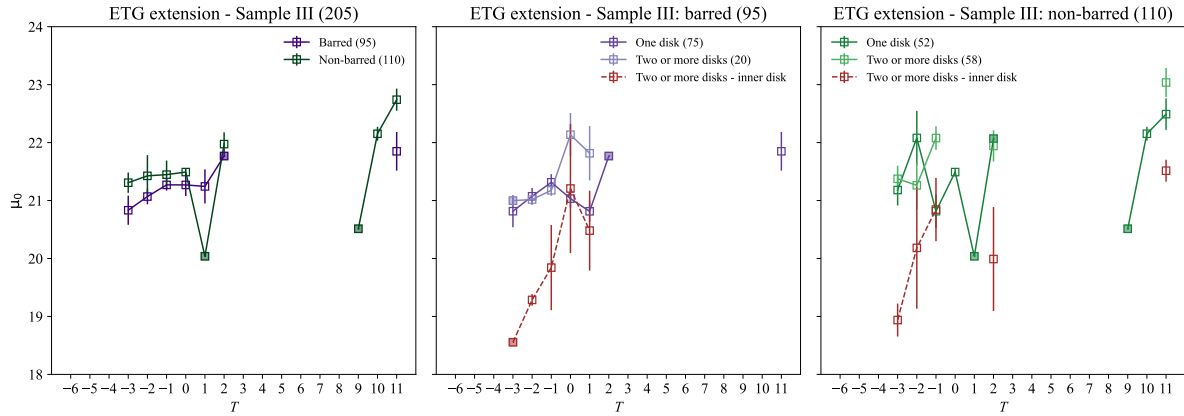
Figure 4.7: Central surface brightness as a function of Hubble type for Sample III of the ETG extension. The first panel compares the values for barred and non-barred galaxies. The second and third panel compares the central surface brightness for models with one or two more disks in the model for barred and non-barred galaxies, respectively. Symbols as in Figure 4.3. Non-dashed lines indicate the behaviour of the only disk in the model or the outer one, giving that the model contains more than one exponential disk. The dashed, red lines in the second and third panel indicate the behaviour of inner disk, in models that contain more than one disk.

21

4.2 ETG versus S^{4}G

Figure 4.8: T-type ocurrences in the S^{4}G + ETG final sample.

In addition to the analysis of the ETG galaxies, a comparison between those and the ones in the S^{4}G original survey is also presented. Galaxies in the S^{4}G with quality flags QF=1 and QF=2 were excluded from the analysis, as well as those containing an e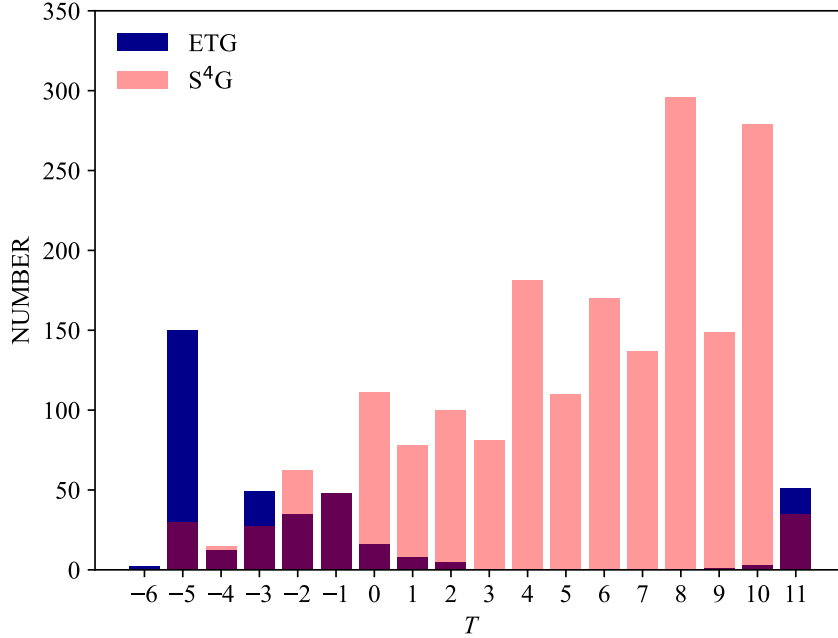dge-on disk, resulting in a sub-set of 1909 galaxies. The S^{4}G + ETG final sample consists of 2289 galaxies, with T-types distributed as seen in Figure 4.8. The lack of types earlier than $T = 0$ is notable for the S^{4}G.

Name	Parameter	Number of galaxies
S^{4}G + ETG extension - Sample I	Bulge luminosity fraction (galaxies with at least a bulge or nucleus component)	1287
S^{4}G + ETG extension - Sample II	Bar luminosity fraction (galaxies with at least a bar component)	676
S^{4}G + ETG extension - Sample III	Disk scale length and central surface brightness (galaxies with at least a disk component)	2083

Table 4.3: Samples of S^{4}G + ETG galaxies used in the analysis. The name, the parameter that it was selected to study and the number of galaxies in the sample is indicated.

As for the analysis of the ETGs on their own, the comparison between the two surveys calls for the creation of different samples. The name and reasoning behind each sample will be specified in the corresponding Subsections, but Table 4.3 summarizes the samples used for the ETG analysis.

4.2.1 Bulge to total luminosity

The bulge luminosity fraction for galaxies of the S^{4}G original sample were obtained following the same procedure explained in Subsection 4.1.1, resulting in a sample of 955 galaxies. The results are shown in Figure 4.9, as well as the values calculated for the ETG extension (previously discussed in Subsection 4.1.1). The merging of both samples results in another one of 1287 galaxies, called S^{4}G + ETG - Sample I. For types $T = -5$ and $T = -4$, B/T values are significantly higher for ETG galaxies. The explanation for the low B/T values for S^{4}G galaxies in these two stages is the following. P4 accounts for 26 elliptical galaxies, all of which were assigned a one-component final model, "B", containing one Sérsic function, but in reality there are 45 galaxies with $T = -5$ and $T = -4$. Those "excess" galaxies (presumably disky

ellipticals) were modelled with a combination of bulge and disk, so the mean bulge luminosity fraction for those stages will be necessarily smaller than unity. On the other hand, for the ETG extension only bulge and nucleus components were used for galaxies with $T = -5$ and $T = -4$. These differences, ultimately based on the differences on the modeling criteria and not the nature of the galaxies, is further supported by the division of the galaxies contained in the S⁴G + ETG - Sample I according to the number of disks. The first panel of the bottom row of Figure 4.10 shows galaxies of the aforementioned sample which models do not contain neither disks nor a bar. The 26 S⁴G elliptical galaxies are included there, with B/T values more consistent with those obtained for the ETG extension galaxies. However, there are also $T = -5$ and $T = -4$ S⁴G galaxies that were modelled using one disk (second panels of the top and bottom row of Figure 4.10, for barred and non-barred, respectively) or even two or more disks (third panel of the bottom row Figure 4.10).
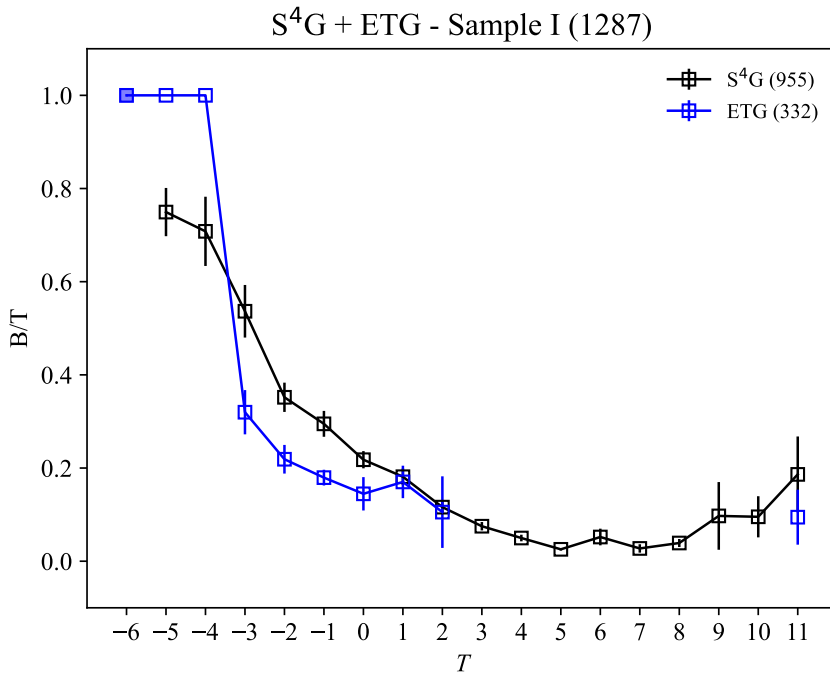

Figure 4.9: Bulge luminosity fraction as a function of Hubble type for Sample I of the S⁴G original sample and the ETG extension. Symbols as in Figure 4.3

The behaviour of the bulge luminosity fraction changes from types ranging from $T = -3$ to $T = 0$: the values are higher for the S⁴G galaxies. This shift, however, can also be attributed to the manner in which the final models were chosen. Once again, Figure 4.10 provides a useful insight into this problem. The bulge luminosity fraction for barred galaxies with one disk in the model (second panel of the top row) appear to be similar. This also applies for those non-barred and with two or more disks in the model (third panel of the bottom row). The differences in B/T arise from non-barred galaxies with one disk in the model (second panel of the bottom row). There is a clear excess of S⁴G galaxies that contain one disk in the model, rather than two or more, when compared to the ETGs. The second (or even third) disk used in the ETG models were occasionally used to model inner regions of the galaxy, which would decrease the luminosity associated to the bulge. The models of the S⁴G are simpler (meaning less components, including disks), so the bulge luminosity may be over-estimated, hence the excess in B/T.
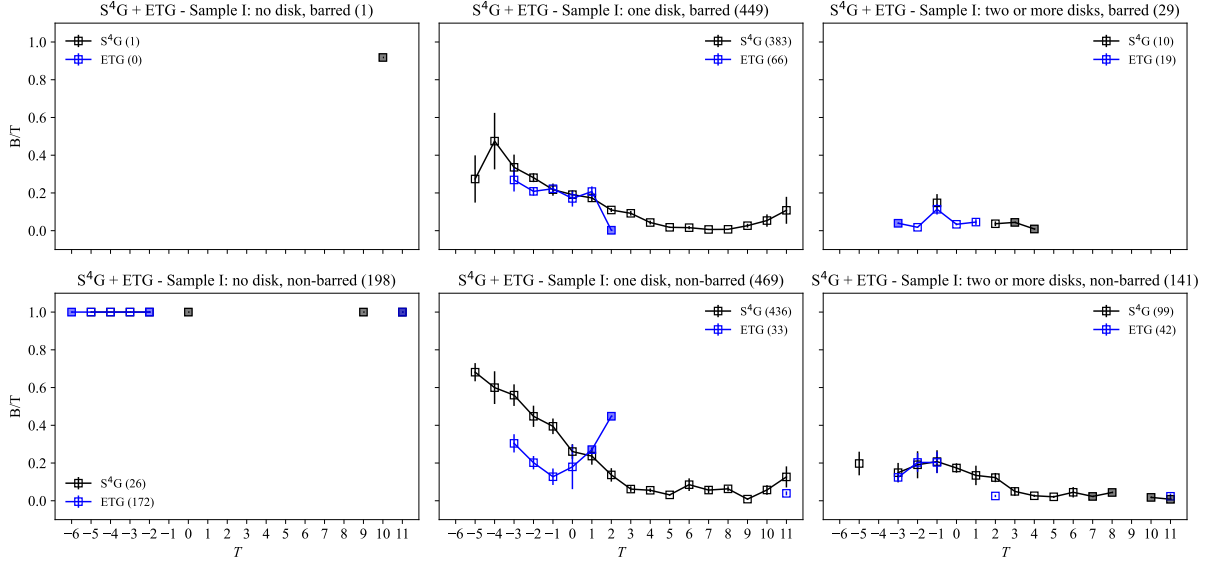
Figure 4.10: Bulge luminosity fraction as a function of Hubble type for Sample I of the S^4G original sample and the ETG extension. Panels in the top row are for barred galaxies, from left to right: galaxies with no disk; galaxies with one disk, and galaxies with two or more disks in the model. The bottom panels are the same but for non-barred galaxies. Symbols as in Figure 4.3

4.2.2 Bar to total luminosity

The bar luminosity fraction for galaxies in the S^4G original sample were calculated following the methodology explained in Subsection 4.1.2, resulting in a sample of 581 galaxies. The outcome is shown in Figure 4.11, as well as the values calculated previously for the ETG extension. The merging of both samples is another one of 676 galaxies, called S^4G + ETG - Sample II. The Bar/T values for T-types ranging from $T = -3$ to $T = -2$ appear to be higher for ETG galaxies than for the S^4G sample, but no other trends can be discerned. Additionally, when comparing with the origial S^4G survey, the bar luminosity fractions for galaxies in the ETG extension do not seem to be affected by the number of disks included in the decompositions, meaning that the bars were adequately modelled regardless of the additional components included in the final model (see Figure 4.12).

It is worth mentioning the recurrence of barred galaxies in both surveys, in particular in the range between types $T = -3$ and $T = 2$. For this span of stages, only 155 of the 426 galaxies (around 37%) of the S^4G survey present a bar, whereas for the ETG extension, 95 of 161 (around 60%) are barred. The explanation for this could be the following. Bars drive gas inflow into the center of galaxies, promoting the growth of bulges/pseudobulges. In Subsection 4.2.1 it was shown that B/T values are higher for S^4G than for ETG galaxies (at least in $T = -3$ and $T = -2$). Assuming that this behaviour is not influenced by the modelling criteria, the S^4G larger bulges could be affecting the bar presence: the growth of the bulge by gas inflow could weaken and eventually dissolve this structure (Shen & Sellwood 2004).

24

Figure 4.11: Bar luminosity fraction as a function of Hubble type for Sample II of the S^{4}G original sample and the ETG extension. Symbols as in Figure 4.3.
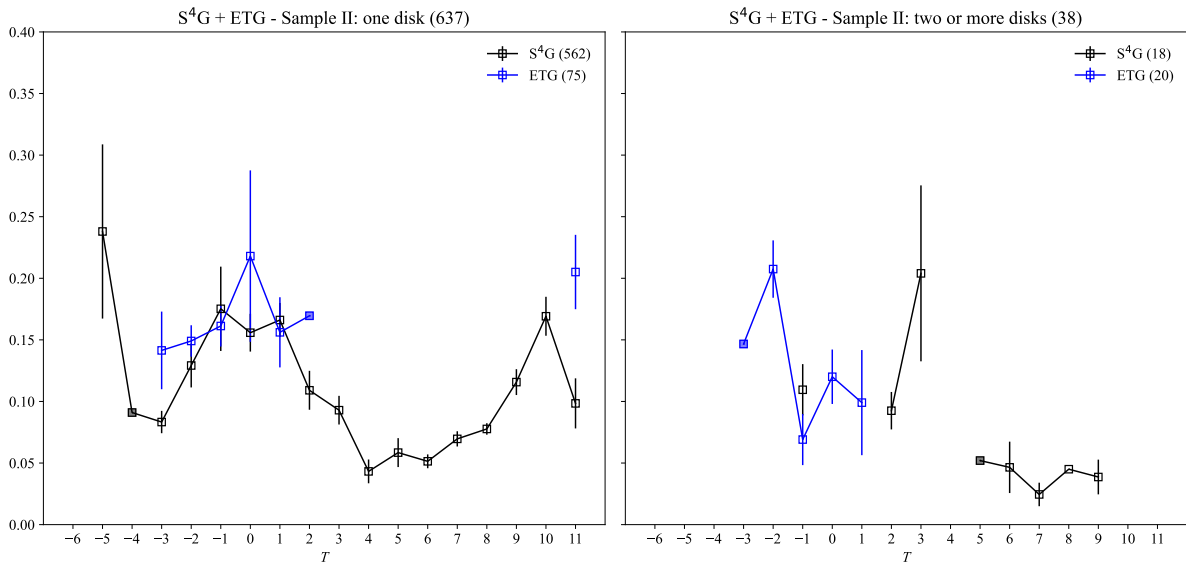
Figure 4.12: Bar luminosity fraction as a function of Hubble type for Sample II of the S^{4}G original sample and the ETG extension. The first panel shows galaxies with disk, the second those with one disk and the third those with two or more disks in the model. Symbols as in Figure 4.3.

4.2.3 Disk properties

The disk scale length and central surface brightness for S^{4}G galaxies were obtained using the same methodology as for the ETG extension (see Subsection 4.1.3). S^{4}G + ETG - Sample III is the result of the merging of the two sub-sets.
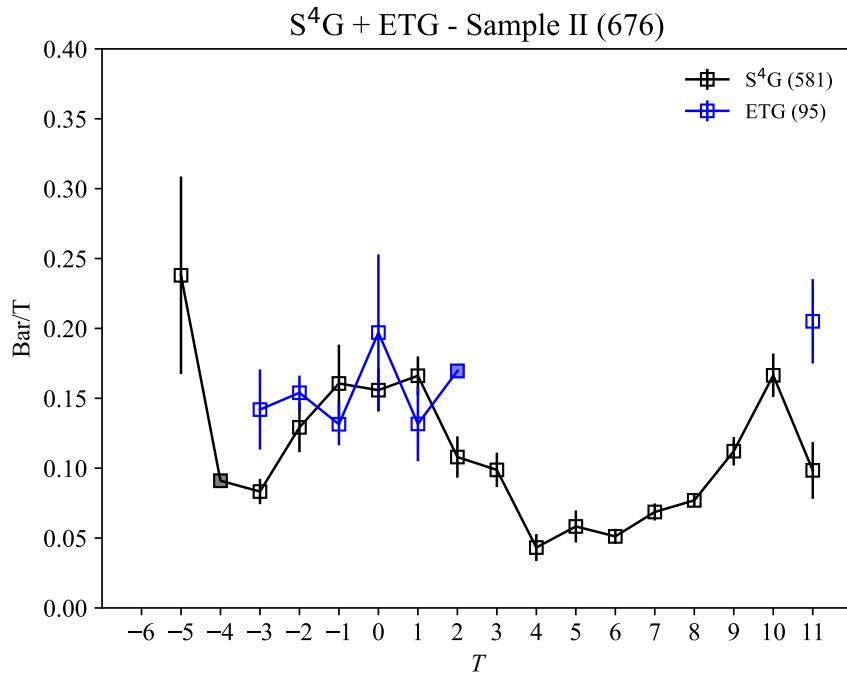
25

Figure 4.13: Disk scale length as a function of Hubble type for Sample III of the S^{4}G original sample and the ETG extension. Symbols as in Figure 4.3. Non-dashed lines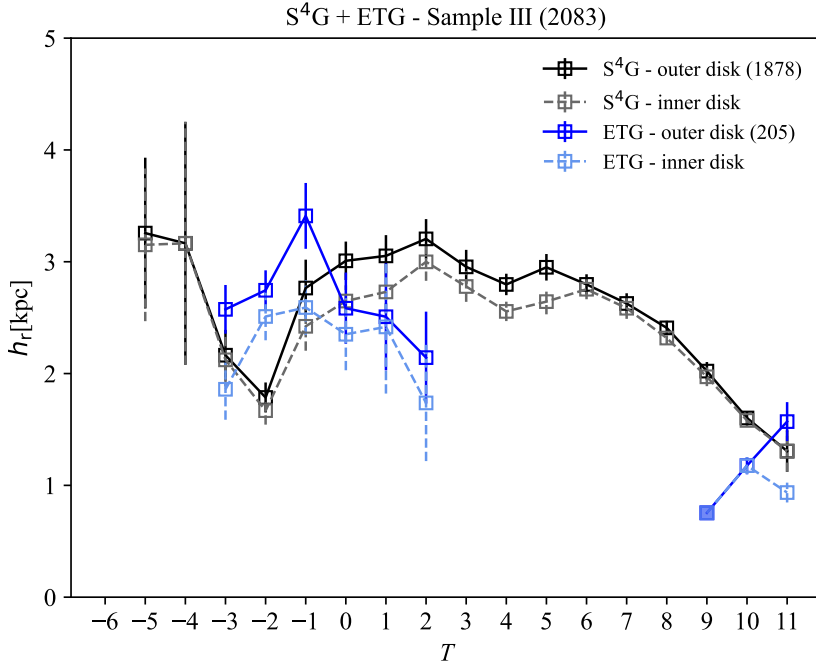 indicate the behaviour of the only disk in the model or the outer one, giving that the model contains more than one exponential disk. The dashed lines indicate the behaviour of the only disk in the model or the inner one, if the model contains more than one disk.

Studies of deep optical and Near Infrared surveys show that approximately a third of galactic disks are simple exponentials (e.g, Erwin et al. 2005; Gutiérrez et al. 2011). The deviations from this behaviour are described with an additional exponential with a different slope (although the brightness profile can sometimes be modelled with three different exponentials): Type II breaks are associated with steeper outer profiles, and Type III breaks to shallower ones. Figure 4.16, taken from Laine et al. (2014) shows these types of profiles for example galaxies of the S^{4}G survey. The models presented in P4 use single exponentials for the disk as a default. However, two exponentials were used when it was strictly necessary. For the ETG extension, the use of two disks (or even three in a couple of cases) is more common and not as restricted. Models for these galaxies usually show a Type III profile. One inconvenience of this approach is that the outer regions of barred early-type galaxies can sometimes be dominated by outer rings (Laine et al. 2014). Erwin et al. (2007) discussed that in some galaxies with outer rings, the break radius of a Type II profile (which cannot be modelled with GALFIT) is similar to the radius of the outer ring, affecting the outer brightness profile.

Figure 4.13 shows the values of the disk scale lengths for barred and non-barred galaxies, for the only disk in the galaxy or the outer one, in case there was more than one disk in the model (non-dashed values). As a comparison, the values for the only disk or the inner one (again, in case of more than one disk in the model) are included (dashed values). Values for the S^{4}G survey in the range $-3 < T < 0$, for the inner disk, are quite similar to those for the outer disks but there is a noticeable drop in the range $0 < T < 6$. This could mean that for types earlier than $T < 0$ in the original sample, there are more galaxies modelled using a single exponential disk, as the variation in scale length is less pronounced. If the models contain more than one exponential disk, the derived scale lengths will vary based on the selection of the inner or the outer disk for the analysis, which is the reason for the difference in values in the range $0 < T < 6$. Figure 4.15b shows the difference in scale lengths for the inner and outer disks
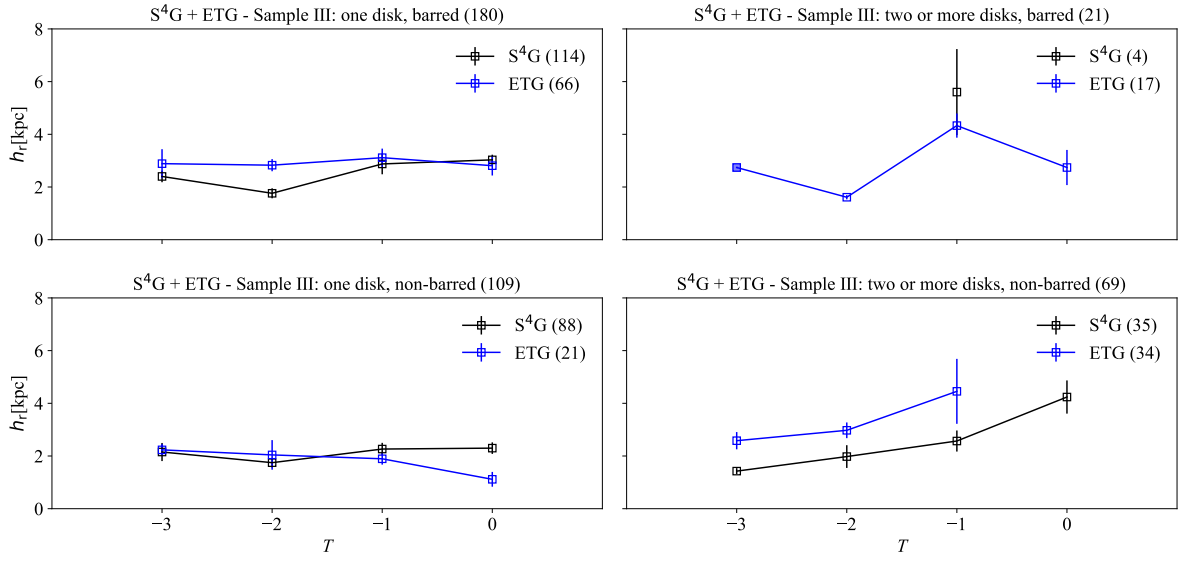
Figure 4.14: Disk scale length as a function of Hubble type for Sample III of the S⁴G original sample and the ETG extension, centered in types $-3 < T < 0$. The first panels in the top and bottom rows compare the values between barred and non-barred galaxies with one disk, respectively. The second panels in the both rows compare the values between barred and non-barred galaxies but with two or more disks, respectively. Values are derived for the only disk in the model or the outer disk, if there are two or more disks present in the model. Symbols as in Figure 4.3.
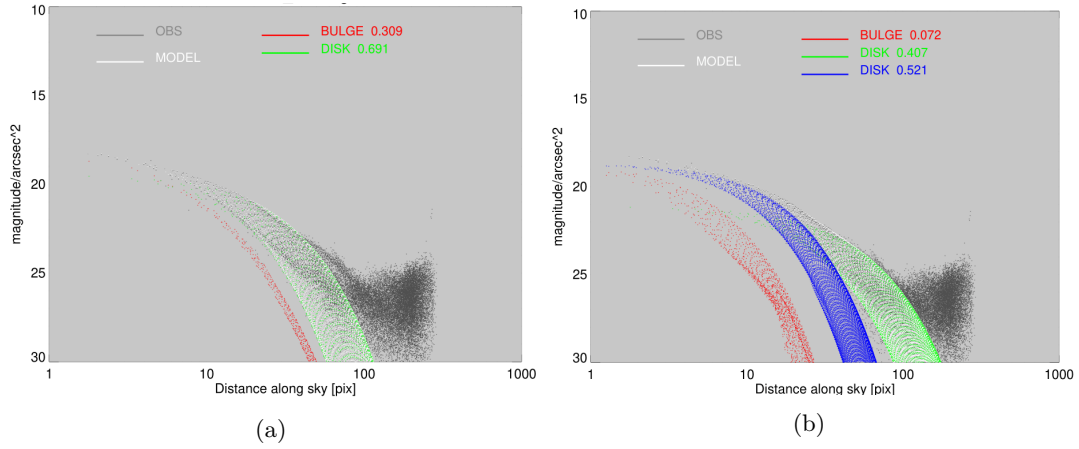
Figure 4.15: a) NGC 1428 model with one disk and b) final model with two disks. Adding an additional inner disk increases the scale length and lowers the central surfae brightness of the main (outer) disk. NGC1428 is a $T = -3$ and QF=5 galaxy from the ETG extension.

for an example galaxy, to illustrate this point. For the ETG extension the decrease in scale length is ubiquitous when using the inner disk for the analysis. This proves that the use of an additional disk is commonplace all throughout the extension: if not, the scale lengths would be similar regardless of the selection of the inner or outer disk for the analysis.

Hereafter, the analysis will be centered in the outer disks, that here is considered the "main disk", as their orientation is fixed to the outer isophotes determined from the original images of the galaxies. Also, only galaxies with T-types between $T = -3$ and $T = 0$ will be considered, as the number of galaxies in the ETG sample is quite low for stages between $T = 0$ and $T = 2$. Figure 4.13 shows that the disk

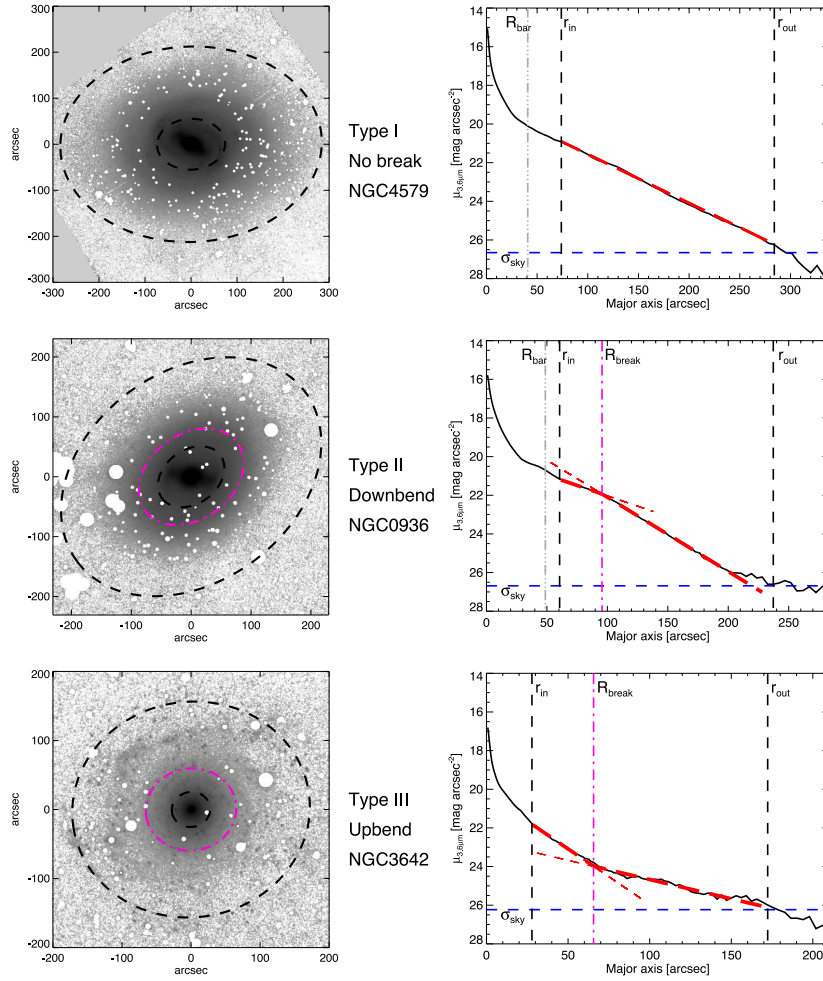Figure 4.16: Image taken from Laine et al. (2014). The different types of disk breaks are depicted, using example galaxies of the S⁴G extension. The Type I disk (no break, top panels) is modelled with a single exponential function (dashed red line). The Type II (downbend, middle panels) and Type III (upbend, bottom panels) disks are modelled using two exponential disks (red dashed lines).

scale lengths for the outer disks appear to be larger than for the original sample, at least in the specified T-type range.

Figure 4.14 shows the difference in the number of models with two disks for the S⁴G + ETG - Sample III. For $-3 < T < 0$, around 40% of ETG galaxies in this sample are modelled using two disks, while only 15% of S⁴G galaxies are modelled this way. The first panel of the top row of Figure 4.14 shows the scale length values for barred galaxies with only one disk in the model. Again, disk scale lengths for ETG galaxies seem to be larger than for S⁴G galaxies. The bar luminosity fractions analysed in Subsection 4.1.2 indicate that for $T = -3$ and $T = -2$ galaxies, Bar/T values are larger for the ETG sample, so this could be influencing the length of the disks, as discussed in Subsection 4.1.3: the mass redistribution triggered by the bar can increase the disk scale length of the host galaxy (e.g, Hohl 1971; Athanassoula & Misiriotis 2002). For non-barred galaxies with one disk (first bottom panel), the values are similar for both surveys, supporting this explanation.

Central surface brightness levels of barred and non-barred galaxies, for the only disk in the galaxy or the outer one in case there was more than one disk in the model (non-dashed values) are shown in Figure 4.17. Values for the only disk or the inner one (in case of more than one disk in the model) are also
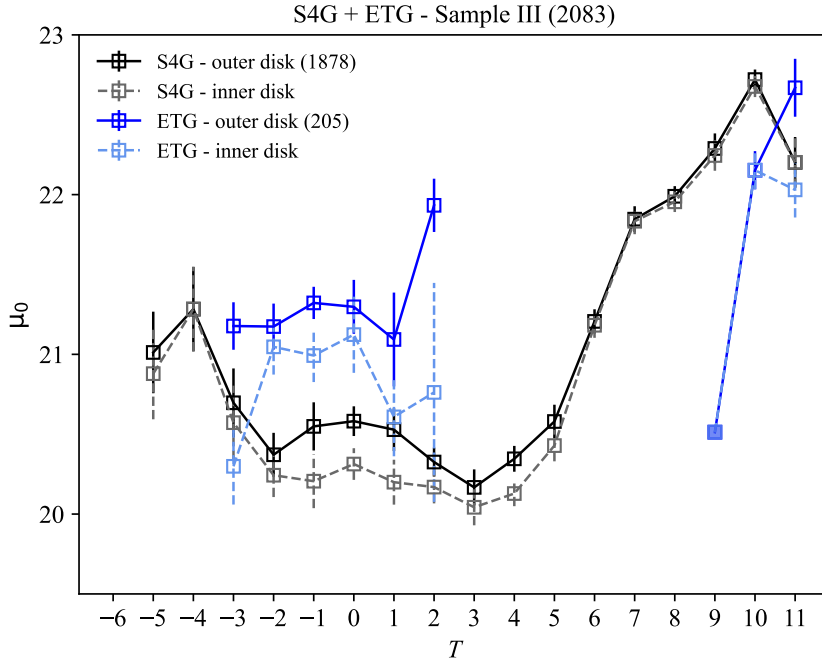
Figure 4.17: Central surface brightness as a function of Hubble type for Sample III of the S^{4}G original sample and the ETG extension. Symbols as in Figure 4.3. Non-dashed lines indicate the behaviour of the only disk in the model or the outer one, giving that the model contains more than one exponential disk. The dashed lines indicate the behaviour of the only disk in the model or the inner one, if the model contains more than one disk.

.

included for comparison (dashed values). Central surface brightness levels are higher for S^{4}G galaxies than for the ETGs, with no dependence on the outer or inner disk for the analysis. This could mean that galaxies in the ETG extension are fainter than those in the S^{4}G original survey. The analysis of the central surface brightness is also centered in T-types between $T = 3$ and $T = 0$ and for the outer disks. Figure 4.18 shows that central surface brightness values are higher for S^{4}G galaxies than for ETGs, independently of the number of disks used in the model and the presence or absence of a bar. For models with two or more disks (at least for the non-barred, second bottom panel of Figure 4.18), it is reasonable that central surface brightness of the ETGs is lower because the additional disks have a larger scale length. This behaviour is illustrated in Figure 4.15b: the addition of an inner disk increases the scale length and lowers the central surface brightness of the main (outer) disk.

Overall, the central surface brightness values appear to be brighter for S^{4}G galaxies. This behaviour is also noted when comparing the absolute magnitude (at 3.6 μm) (see Figure 4.19) as a function of T-type and for galaxies of the S^{4}G + ETG - Sample III between $-3 < T < 0$. This trend could be a direct consequence of dealing with gas-poor and gas-rich galaxies. S^{4}G galaxies, which are gas-rich, could still be experiencing star formation and this would increase the different brightness values. In near infrared wavelengths, light can be affected by young stars (Rhoads 1998), although much less than in the optical range.
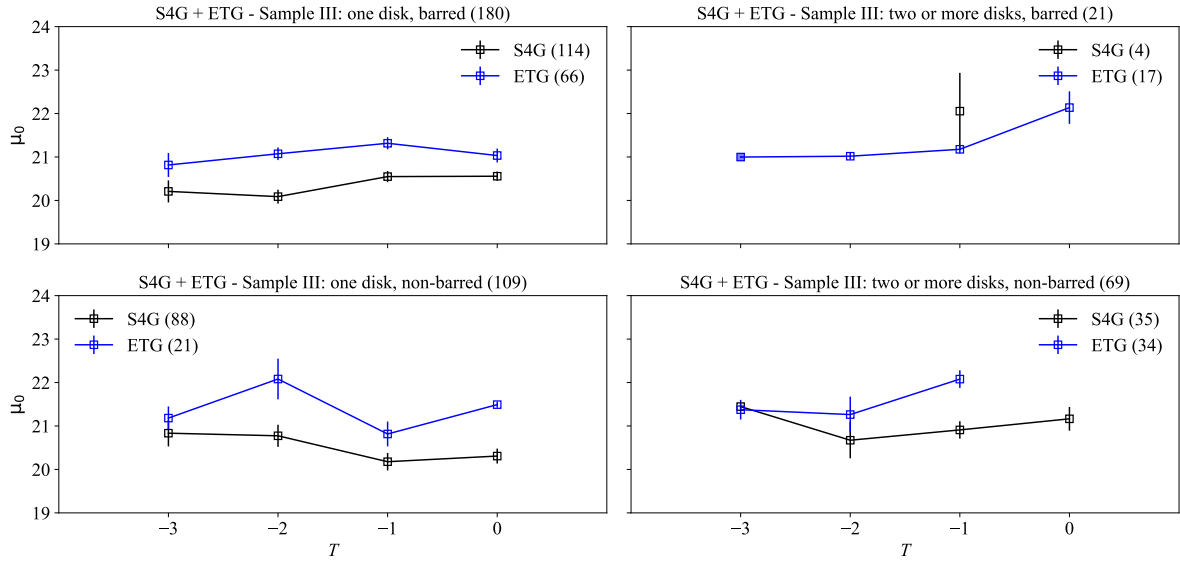
Figure 4.18: Central surface brightness as a function of Hubble type for Sample III of the S^4G original sample and the ETG extension, centered in types $-3 < T < 0$. The first panels in the top and bottom rows compare the values between barred and non-barred galaxies with one disk, respectively. The second panels in the both rows compare the values between barred and non-barred galaxies but with two or more disks, respectively. Values are derived for the only disk in the model or the outer disk, if there are two or more disks present in the model. Symbols as in Figure 4.3.

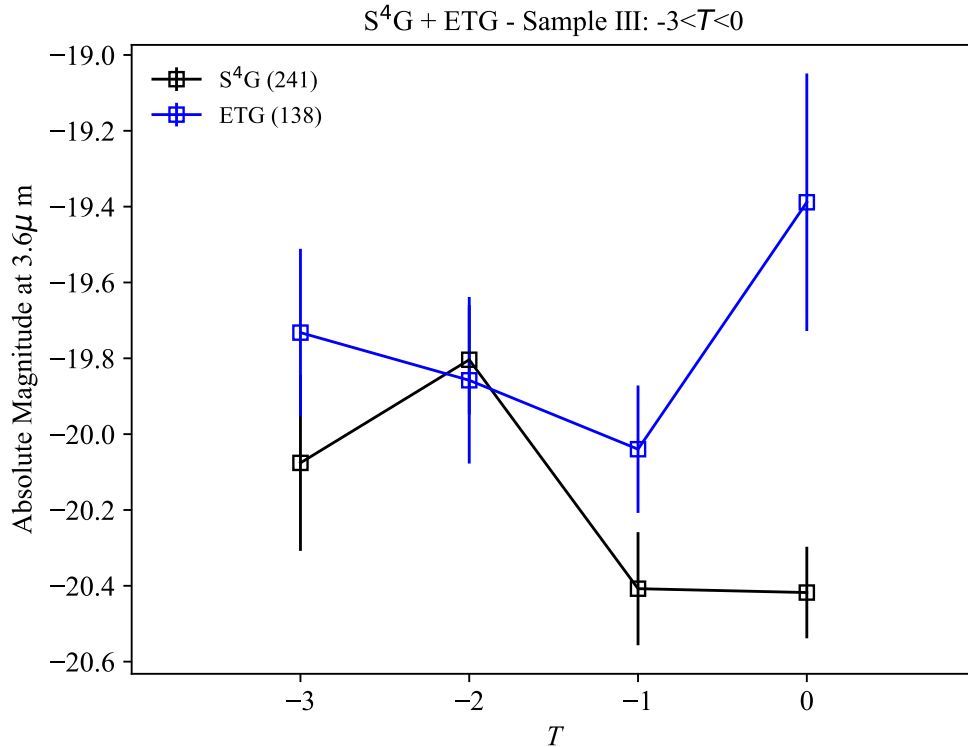Figure 4.19: Absolute magnitude at 3.6 μm as a function of Hubble type for Sample III of the S^4G original sample and the ETG extension, centered in types $-3 < T < 0$. Symbols as in Figure 4.3.

Chapter 5

Conclusions and future work

The 2D photometric decompositions for the ETG extension of the S^{4}G survey have been performed using GALFIT, for the 3.6 μm images. All of them were assigned a quality flag (QF) ranging from 1 to 5, depending on the reliability of the model. Those with a QF=1 and 2 were excluded from further analysis, as well as the galaxies with an edge-on orientation. The final sample consists of 380 galaxies, for which some structural parameters were derived and averaged for each Hubble type: the bulge luminosity fraction, the Sérsic index, the bar luminosity fraction, and the disks' scale length and central surface brigthness. These results have been discussed on their own, but a comparison with the galaxies of the original S^{4}G survey is also provided.

The main results for the ETG extension analysis are:

(i) Pseudo-bulges could be present in the ETG extension galaxies with $T > -3$. In barred galaxies, parts of said pseudobulges could blend with the bar, affecting the bulge luminosity fraction, as discussed in Laurikainen et al. (2007).

(ii) The bar luminosity fractions for the available T-types fall into the same range, approximately, between 0.10 and 0.20, but without a significant trend.

(iii) In case that the final model contained more than one exponential disk, the outer one was selected for the analysis for deriving the disk scale length and central surface brightness. A comparison with the values for the inner disks is given, to illustrate that the outer ones were used to model the outer regions of the galaxies, and thus present larger scale lengths and lower brightness levels.

(iv) For the outer disks, the disk scale lengths appear to be larger for barred galaxies than for their non-barred counterparts. The presence of a bar could be influencing this result: the mass redistribution triggered by this structure can increase the disk scale length of the host galaxy (e.g, Hohl 1971; Athanassoula & Misiriotis 2002).

(v) The central surface brightness values of barred galaxies are higher. This could be a consequence of bar-driven gas inflow toward the center of galaxies, which triggers star formation (e.g, Lin et al. 2017), and as shown by nuclear rings of star formation (Comerón et al. 2010).

The comparison between the ETG extension and the original S^{4}G survey resulted in the following conclusions:

(i) The bulge luminosity fraction is lower for S^{4}G galaxies than for the ETG galaxies in the $T = -5$ and $T = -4$ stages. This is because for the original survey, a significant number of those galaxies were modelled with a combination of bulge and disk, whereas for the ETG models for ellipticals only bulge and nucleus components were used. This behaviour shifts for $-3 < T < 0$. The reason for this is that ETG extension models sometimes contain two exponential disks and the inner-most one

31

could be "robbing" luminosity that in the S^{4}G galaxies (where models with two disks components are less common) in usually attributed to the bulge.

(ii) Bar luminosity fractions appear to be higher for ETG galaxies than for the ones included in the original survey for types $T = -3$ and $T = -2$. This could be a consequence of the presence of larger bulges/pseudobulges for said T-types in the S^{4}G survey: the growth of the bulge/pseudobulge promoted by bar-driven gas inflow could eventually weaken and dissolve the bar, as discussed in Shen & Sellwood (2004).

(iii) Disk parameters (the scale length and central surface brightness) are influenced by the different modelling criteria used when making the decompositions of both surveys. In P4 of the S^{4}G original survey, it is considered that one disk is enough to estimate both disk parameter. For the ETG extension, however, the use of additional exponential disks was encouraged. For this reason, disk scale lengths appear to be larger and brightness surface values are fainter for the ETG galaxies (although this could also mean that the extension galaxies are fainter than the ones in the original survey).

(iv) The comparison of absolute magnitude at 3.6 μm for galaxies in both surveys in the T-type range $-3 < T < 0$ confirms that ETG galaxies are fainter than those in the S^{4}G original survey. This could be a consequence of the S^{4}G galaxies having more gas, and therefore more star formation than the ETG extension galaxies.

The differences in the modelling criteria could be a potential issue when a comprehensive analysis of both surveys is established. For this reason, the decompositions of both surveys should be revised and the criteria uniformised. An interesting line of study could be the influence of outer rings on the disk parameters for the ETG extension. Finally, and most importantly, the ETG extension decompositions performed in this work will be an essential contribution to the ultimate release of Pipeline 4 of this survey.

Appendix A

Table example for ETG output parameters

Table A.1: Excerpt of the table containing the ETG extension output parameters. The original table is cropped to fit the page.

	name	model	h_type	flag	phys_psf	frel_psf	phys_s1	mag_s1	re_s1	pa_s1	ar_s1	n_s1	ext
0	NGC0216	dbar	-2.0	5.0	-	0.000000	-	0.0000	0.0000	0.0000	0.0000	0.0000	ext2
1	NGC0357	bdbar	0.0	5.0	-	0.000000	-	12.7520	3.6730	24.1531	0.8746	1.5182	ext2
2	NGC0448	bbn	-3.0	5.0	NUCLEUS	0.026200	BULGE	12.5015	9.6126	-62.3480	0.2837	1.7250	ext2
3	NGC0502	bdd	-1.0	5.0	-	0.000000	BULGE	13.1587	3.4541	-45.1752	0.8535	2.7636	ext2
4	NGC0509	dbarfn	-1.0	5.0	NUCLEUS	0.046887	-	0.0000	0.0000	0.0000	0.0000	0.0000	ext2
5	NGC0524	bdd	-2.0	4.0	-	0.000000	BULGE	11.2772	7.9531	33.8551	0.9665	2.0698	ext2
6	NGC0525	dbarn	0.0	5.0	-	0.073930	-	0.0000	0.0000	0.0000	0.0000	0.0000	ext2
7	NGC0596	bbn	-5.0	5.0	NUCLEUS	0.007779	BULGE	11.1557	15.3662	-75.4762	0.8816	4.0556	ext2
8	NGC0636	bb	-5.0	4.0	NUCLEUS	0.000000	BULGE	10.9386	29.2321	66.6848	0.8731	6.5640	ext2
9	NGC0720	b	-5.0	5.0	-	0.000000	BULGE	9.7580	41.0908	-37.7995	0.5862	3.2677	ext2
10	NGC0821	bbn	-5.0	5.0	-	0.005172	BULGE	11.1151	19.0593	31.4707	0.5431	4.8083	ext2
11	NGC1172	bbn	-5.0	4.0	BULGE	0.037096	BULGE	12.7775	7.2095	32.8847	0.8851	2.3116	ext2
12	NGC1188	dn	11.0	5.0	-	0.120697	-	0.0000	0.0000	0.0000	0.0000	0.0000	ext2
13	NGC1199	bn	-5.0	5.0	BULGE	0.010791	BULGE	10.6223	41.4516	52.5659	0.7231	4.8380	ext2
14	NGC1201	ddn	-3.0	5.0	BULGE	0.035913	-	0.0000	0.0000	0.0000	0.0000	0.0000	ext2
15	NGC1209	b	-5.0	5.0	NUCLEUS	0.000000	BULGE	10.6808	31.5983	82.2874	0.4786	5.0928	ext2
16	NGC1248	dbarn	0.0	5.0	-	0.081458	-	0.0000	0.0000	0.0000	0.0000	0.0000	ext2
17	NGC1289	bn	-5.0	5.0	NUCLEUS	0.069741	BULGE	11.8855	31.4154	-84.0257	0.5815	4.8084	ext2
18	NGC1315	bdbar	-2.0	5.0	NUCLEUS	0.000000	BULGE	13.6757	5.1329	39.8767	0.9363	2.5225	ext2
19	NGC1336	bbn	-5.0	4.0	NUCLEUS	0.036708	BULGE	12.3966	52.1506	21.4917	0.7078	1.9155	ext2
20	NGC1340	b	-5.0	5.0	NUCLEUS	0.000000	BULGE	9.7396	56.5430	-13.9275	0.6575	4.1970	ext2
21	NGC1351	bn	-5.0	5.0	NUCLEUS	0.012224	BULGE	10.8693	53.9584	-39.0957	0.5982	6.3025	ext2
22	NGC1354	ddbarfn	-1.0	5.0	-	0.063614	-	0.0000	0.0000	0.0000	0.0000	0.0000	ext2
23	NGC1362	bn	-5.0	5.0	NUCLEUS	0.109380	BULGE	12.5933	20.9493	10.8655	0.9056	3.0739	ext2
24	NGC1370	bn	-4.0	5.0	NUCLEUS	0.061858	BULGE	12.3642	22.1670	54.2963	0.6194	2.1182	ext2
25	NGC1373	b	-5.0	5.0	-	0.000000	BULGE	12.9626	12.6283	-60.4428	0.7523	5.1801	ext2
26	NGC1374	bb	-5.0	5.0	NUCLEUS	0.000000	BULGE	10.7202	31.1945	-60.5122	0.8924	2.8224	ext2
27	NGC1375	ddn	-3.0	4.0	NUCLEUS	0.036128	-	0.0000	0.0000	0.0000	0.0000	0.0000	ext2
28	NGC1379	bn	-5.0	5.0	NUCLEUS	0.022289	BULGE	10.6164	36.1025	5.6871	0.9729	2.6470	ext2
29	NGC1380	bddbar	-1.0	5.0	NUCLEUS	0.000000	BULGE	11.3222	7.9853	12.0509	0.7849	2.7604	ext2
30	NGC1380B	ddbarn	-2.0	5.0	-	0.016155	-	0.0000	0.0000	0.0000	0.0000	0.0000	ext2
31	NGC1383	bdbarn	0.0	4.0	NUCLEUS	0.025665	BULGE	12.8221	6.3733	79.7219	0.6487	1.4248	ext2
32	NGC1387	bdbar	-3.0	5.0	NUCLEUS	0.000000	BULGE	10.9923	5.6955	-80.1559	0.9687	1.7420	ext2
33	NGC1393	ddbarn	-1.0	5.0	NUCLEUS	0.036573	-	0.0000	0.0000	0.0000	0.0000	0.0000	ext2
34	NGC1395	b	-5.0	5.0	BULGE	0.000000	BULGE	9.1821	65.6447	-84.2222	0.8285	4.4120	ext2
35	NGC1399	bb	-5.0	5.0	BULGE	0.000000	BULGE	10.1043	13.4979	-65.9001	0.8659	1.8716	ext2
36	NGC1400	b	-5.0	5.0	BULGE	0.000000	BULGE	10.1349	31.4378	35.9496	0.8863	5.2824	ext2
37	NGC1403	bbn	-5.0	4.0	NUCLEUS	0.046481	BULGE	13.3831	5.5156	-15.9535	0.3836	2.7002	ext2
38	NGC1407	bbb	-5.0	4.0	-	0.000000	BULGE	11.2701	7.3517	55.0581	0.9499	1.1628	ext2
39	NGC1416	bn	-5.0	5.0	NUCLEUS	0.022703	BULGE	12.4839	46.0541	-34.1040	0.8879	4.3872	ext2
40	NGC1419	b	-5.0	5.0	BULGE	0.000000	BULGE	12.3364	10.4612	-21.2715	0.9762	4.5494	ext2

Appendix B

GALFIT input

```
    =====================================================
# IMAGE and GALFIT CONTROL PARAMETERS
A) NGC0216.phot.1_nonan.fits          # Input data image (FITS file)
B) NGC0216_bdbarnmodel.fits            # Output data image block
C) NGC0216_sigma2015.fits          # Sigma image name (made from data if blank or "none")
D) PSF-1.composite.fits          # PSF image name
E)    5                 # PSF fine sampling factor relative to data
F) NGC0216.1.finmask_nonan.fits           # Bad pixel mask (FITS image or ASCII coord list)
G) none                  # File with parameter constraints (ASCII file)
H)   433    875    517    959             # Image region to fit (xmin xmax ymin ymax)
I) 50    50                # Size of the convolution box (x y)
J) 21.0967                  # Magnitude photometric zeropoint
K) 0.75     0.75          # Plate scale (dx dy)   [arcsec per pixel]
O) regular               # Display type (regular, curses, both)
P) 0                     # Choose: 0=optimize, 1=model, 2=imgblock, 3=subcomps


#-------------------------------------------------------------------
# STRUCTURE:  BULGE
# Sersic function
# Component number: 1
 0) sersic                 #  Component type
 1)   654.983  738.479   0 0       #  Position x, y
 3)    13.883  1        #  Integrated magnitude
 4)    10.430  1          #  R_e (effective radius)   [pix]
 5) 2.0          1         #  Sersic index n (de Vaucouleurs n=4)
 9) 0.9          1         #  Axis ratio (b/a)
 10) 10.0        1         #  Position angle (PA)  [deg: Up=0, Left=90]
 Z) 0                      #  leave in [1] or subtract [0] this comp from data?
#-------------------------------------------------------------------
# STRUCTURE:  DISK
# Exponential function
# Component number: 2
 0) expdisk               #  Component type
 1)  654.983  738.479   0 0     #  Position x, y
 3)   13.883  1        #  Integrated magnitude
 4)      42.5000  1       #  R_s (disk scale-length)   [pix]
 9)     0.385470 0   #  Axis ratio (b/a)
 10)     28.9163 0   #  Position angle (PA) [deg: Up=0, Left=90]
 Z) 0                     #  leave in [1] or subtract [0] this comp from data?
#-------------------------------------------------------------------
```

```
# STRUCTURE:  BAR
# Ferrer-bar
# Component number: 3
 0) ferrer2               #  Component type
 1)  654.983  738.479  0 0     #  Position x, y
 3)   25.125  1          #  surface brghtness at effective radius [mag/arcsec^2]
 4) 50.  1          #  Outer truncation radius  [pix]
 5) 2   0          #  Alpha (outer truncation sharpness)
 6)  0          0          #  Beta (central slope)
 9   0.5          1          #  Axis ratio (b/a)
10)      118.916  1          #  Position angle (PA) [deg: Up=0, Left=90]
 Z)  0                    #  leave in [1] or subtract [0] this comp from data?
#-------------------------------------------------------------
# STRUCTURE:  NUCLEUS
# point source
# Component number: 4
 0) psf                   # Object type
 1)  654.983  738.479   0 0     # Position x, y
 3)   17.883   1         # Integrated magnitude
 Z) 0                     # leave in [1] or subtract [0] this comp from data?
```

Bibliography

Athanassoula, E. & Misiriotis, A. 2002, MNRAS, 330, 35

Bournaud, F., Jog, C. J., & Combes, F. 2007, A&A, 476, 1179

Buta, R., Corwin, H. G., J., & Odewahn, S. C. 2002, in Astronomical Society of the Pacific Conference Series, Vol. 275, Disks of Galaxies: Kinematics, Dynamics and Peturbations, ed. E. Athanassoula, A. Bosma, & R. Mujica, 102

Cappellari, M., Emsellem, E., Krajnović, D., et al. 2011, MRAS, 416, 1680

Comerón, S., Salo, H., & Knapen, J. H. 2018, A&A, 610, A5

Comerón, S., Knapen, J. H., Beckman, J. E., et al. 2010, Monthly Notices of the Royal Astronomical Society, 402, 2462

Daddi, E., Renzini, A., Pirzkal, N., et al. 2005, ApJ, 626, 680

Dekel, A. & Birnboim, Y. 2006, MNRAS, 368, 2

Draine, B. T. & Lee, H. M. 1984, ApJ, 285, 89

Dressler, A. 1980, ApJ, 236, 351

Driver, S. P., Robotham, A. S. G., Bland-Hawthorn, J., et al. 2013, MNRAS, 430, 2622

Eggen, O. J., Lynden-Bell, D., & Sandage, A. R. 1962, ApJ, 136, 748

Erwin, P., Beckman, J. E., & Pohlen, M. 2005, AJ, 626, L81

Erwin, P., Pohlen, M., & Beckman, J. E. 2007, AJ, 135, 20

Falcón-Barroso, J., van de Ven, G., Lyubenova, M., et al. 2019, A&A, 632, A59

Fazio, G. G., Hora, J. L., Allen, L. E., et al. 2004, The Astrophysical Journal Supplement Series, 154, 10

Fisher, D. B. & Drory, N. 2008, AJ, 136, 773

Franx, M., Illingworth, G., & de Zeeuw, T. 1991, ApJ, 383, 112

Gutiérrez, L., Erwin, P., Aladro, R., & Beckman, J. E. 2011, AJ, 142, 145

Hohl, F. 1971, ApJ, 168, 343

Huang, S., Ho, L. C., Peng, C. Y., Li, Z.-Y., & Barth, A. J. 2013, AJ, 766, 47

Hubble, E. P. 1926, ApJ, 64, 321

Hubble, E. P. 1936, Realm of the Nebulae

Kormendy, J. 1977, ApJ, 218, 333

Kormendy, J. 1982, ApJ, 257, 75

Kormendy, J. & Kennicutt, Robert C., J. 2004, ARAA, 42, 603

Laine, J., Laurikainen, E., Salo, H., et al. 2014, MNRAS, 441, 1992

Laurikainen, E., Salo, H., Buta, R., & Knapen, J. 2011, AA, 2011

Laurikainen, E., Salo, H., Buta, R., & Knapen, J. H. 2007, MNRAS, 381, 401

Lin, L., Li, C., He, Y., Xiao, T., & Wang, E. 2017, AJ, 838, 105

Muñoz-Mateos, J. C., Sheth, K., Regan, M., et al. 2015, ApJS, 219, 3

Oser, L., Ostriker, J. P., Naab, T., Johansson, P. H., & Burkert, A. 2010, AJ, 725, 2312

Pahre, M. A., Ashby, M. L. N., Fazio, G. G., & Willner, S. P. 2004, ApJS, 154, 229

Paturel, G., Petit, C., Prugniel, P., et al. 2003, AAP, 412, 45

Peletier, R. F., Kutdemir, E., van der Wolk, G., et al. 2012, MNRAS, 419, 2031

Peng, C. Y., Ho, L. C., Impey, C. D., & Rix, H.-W. 2002, The Astronomical Journal, 124, 266

Peng, C. Y., Ho, L. C., Impey, C. D., & Rix, H.-W. 2010, The Astronomical Journal, 139, 2097

Querejeta, M., Eliche-Moral, M. C., Tapia, T., et al. 2015a, A&A, 579, L2

Querejeta, M., Meidt, S. E., Schinnerer, E., et al. 2015b, ApJS, 219, 5

Regan, M. W. 2013, in American Astronomical Society Meeting Abstracts, Vol. 221, American Astronomical Society Meeting Abstracts #221, 230.02

Rhoads, J. E. 1998, AJ, 115, 472

Ryan, R. E., McCarthy, P. J., Cohen, S. H., et al. 2012, ApJ, 749, 53

Salo, H., Laurikainen, E., Laine, J., et al. 2015, ApJS, 219, 4

Shen, J. & Sellwood, J. A. 2004, AJ, 604, 614

Sheth, K., Armus, L., Athanassoula, E., et al. 2013, Not Dead Yet! Completing Spitzer's Legacy with Early Type Galaxies, Spitzer Proposal ID 10043

Sheth, K., Regan, M., Hinz, J. L., et al. 2010, PASP, 122, 1397

van den Bergh, S. 1976, ApJ, 206, 883

Watkins, A. E., Salo, H., Laurikainen, E., et al. 2022, Stellar masses, sizes, and radial profiles for 465 nearby early-type galaxies: an extension to the Spitzer Survey of Stellar Structure in Galaxies (S^4G)

Werner, M. W., Roellig, T. L., Low, F. J., et al. 2004, AJSS, 154, 1